

# ANTARES<sup>☆</sup>: the first undersea neutrino telescope

M. Ageron<sup>a</sup>, J.A. Aguilar<sup>b</sup>, I. Al Samarai<sup>a</sup>, A. Albert<sup>c</sup>, F. Ameli<sup>d</sup>,  
M. André<sup>e</sup>, M. Anghinolfi<sup>f</sup>, G. Anton<sup>g</sup>, S. Anvar<sup>h</sup>, M. Ardid<sup>i</sup>, K. Arnaud<sup>a</sup>,  
E. Aslanides<sup>a</sup>, A.C. Assis Jesus<sup>j</sup>, T. Astraatmadja<sup>j,1</sup>, J.-J. Aubert<sup>a</sup>,  
R. Auer<sup>g</sup>, E. Barbarito<sup>k</sup>, B. Baret<sup>l</sup>, S. Basa<sup>m</sup>, M. Bazzotti<sup>n,o</sup>, Y. Becherini<sup>p</sup>,  
J. Beltramelli<sup>h</sup>, A. Bersani<sup>f</sup>, V. Bertin<sup>a</sup>, S. Beurthey<sup>a</sup>, S. Biagi<sup>n,o</sup>,  
C. Bigongiari<sup>b</sup>, M. Billault<sup>a</sup>, R. Blaes<sup>c</sup>, C. Bogazzi<sup>j</sup>, N. de Botton<sup>p</sup>,  
M. Bou-Cabo<sup>i</sup>, B. Boudahef<sup>q</sup>, M.C. Bouwhuis<sup>j</sup>, A.M. Brown<sup>a</sup>, J. Brunner<sup>a,2</sup>,  
J. Busto<sup>a</sup>, L. Caillat<sup>a</sup>, A. Calzas<sup>a</sup>, F. Camarena<sup>i</sup>, A. Capone<sup>d,r</sup>,  
L. Caponetto<sup>s</sup>, C. Cârloganu<sup>t</sup>, G. Carminati<sup>n,o</sup>, E. Carmona<sup>b</sup>, J. Carr<sup>a</sup>,  
P.H. Carton<sup>h</sup>, B. Cassano<sup>k</sup>, E. Castorina<sup>q,u</sup>, S. Cecchini<sup>o</sup>, A. Ceres<sup>k</sup>,  
Th. Chaleil<sup>h</sup>, Ph. Charvis<sup>v</sup>, P. Chauchot<sup>w</sup>, T. Chiarusi<sup>o</sup>, M. Circella<sup>k,\*\*</sup>,  
C. Compère<sup>w</sup>, R. Coniglione<sup>x</sup>, X. Coppolani<sup>h</sup>, A. Cosquer<sup>a</sup>, H. Costantini<sup>f</sup>,  
N. Cottini<sup>p</sup>, P. Coyle<sup>a</sup>, S. Cuneo<sup>f</sup>, C. Curtil<sup>a</sup>, C. D'Amato<sup>x</sup>, G. Damy<sup>w</sup>,  
R. van Dantzig<sup>j</sup>, G. De Bonis<sup>d,r</sup>, G. Decock<sup>h</sup>, M.P. Decowski<sup>j</sup>, I. Dekeyser<sup>y</sup>,  
E. Delagnes<sup>h</sup>, F. Desages-Ardellier<sup>h</sup>, A. Deschamps<sup>v</sup>, J.-J. Destelle<sup>a</sup>,  
F. Di Maria<sup>g</sup>, B. Dinkespiler<sup>a</sup>, C. Distefano<sup>x</sup>, J.-L. Dominique<sup>h</sup>,  
C. Donzaud<sup>l,p,z</sup>, D. Dornic<sup>a,b</sup>, Q. Dorosti<sup>aa</sup>, J.-F. Drogou<sup>ab</sup>, D. Drouhin<sup>c</sup>,  
F. Druillolle<sup>h</sup>, D. Durand<sup>h</sup>, R. Durand<sup>h</sup>, T. Eberl<sup>g</sup>, U. Emanuele<sup>b</sup>,  
J.J. Engelen<sup>j</sup>, J.-P. Ernenwein<sup>a</sup>, S. Escoffier<sup>a</sup>, E. Falchini<sup>q,u</sup>, S. Favard<sup>a</sup>,  
F. Fehr<sup>g</sup>, F. Feinstein<sup>a,p</sup>, M. Ferri<sup>i</sup>, S. Ferry<sup>p</sup>, C. Fiorello<sup>k</sup>, V. Flaminio<sup>q,u</sup>,  
F. Folger<sup>g</sup>, U. Fritsch<sup>g</sup>, J.-L. Fuda<sup>y</sup>, S. Galatá<sup>a</sup>, S. Galeotti<sup>q,u</sup>, P. Gay<sup>t</sup>,  
F. Gensolen<sup>a</sup>, G. Giacomelli<sup>n,o</sup>, C. Gojak<sup>a</sup>, J.P. Gómez-González<sup>b</sup>,

---

<sup>☆</sup>Astronomy with a Neutrino Telescope and Abyss environmental RESearch

\*Corresponding author. Postal address: CE Saclay, Bât.141, 91191 Gif-sur-Yvette, France

\*\*Corresponding author. Postal address: INFN Sezione di Bari, via Amendola 173, 70126 Bari, Italy

*Email addresses:* Marco.Circella@ba.infn.it (M. Circella),  
jean-pierre.schuller@cea.fr (J.-P. Schuller)

<sup>1</sup>Also at University of Leiden, the Netherlands

<sup>2</sup>On leave at DESY, Platanenallee 6, D-15738 Zeuthen, Germany

<sup>3</sup>Now at Bergische Universität Wuppertal, Fachbereich C - Mathematik und Naturwissenschaften, 42097 Wuppertal

<sup>4</sup>Now at IRFU/DSM/CEA, CE Saclay, 91191 Gif-sur-Yvette, France

<sup>5</sup>Deceased (December 2010).

Ph. Goret<sup>ac</sup>, K. Graf<sup>g</sup>, G. Guillard<sup>ad</sup>, G. Halladjian<sup>a</sup>, G. Hallewell<sup>a</sup>,  
H. van Haren<sup>ae</sup>, B. Hartmann<sup>g</sup>, A.J. Heijboer<sup>j</sup>, E. Heine<sup>j</sup>, Y. Hello<sup>v</sup>,  
S. Henry<sup>a</sup>, J.J. Hernández-Rey<sup>b</sup>, B. Herold<sup>g</sup>, J. Hößl<sup>g</sup>, J. Hogenbirk<sup>j</sup>,  
C.C. Hsu<sup>j</sup>, J.R. Hubbard<sup>p</sup>, M. Jaquet<sup>a</sup>, M. Jaspers<sup>j,af</sup>, M. de Jong<sup>j,1</sup>,  
D. Jourde<sup>h</sup>, M. Kadler<sup>ag</sup>, N. Kalantar-Nayestanaki<sup>aa</sup>, O. Kalekin<sup>g</sup>,  
A. Kappes<sup>g</sup>, T. Karg<sup>g,3</sup>, S. Karkar<sup>a</sup>, M. Karolak<sup>h</sup>, U. Katz<sup>g</sup>, P. Keller<sup>a</sup>,  
P. Kestener<sup>h</sup>, E. Kok<sup>j</sup>, H. Kok<sup>j</sup>, P. Kooijman<sup>j,af,ah</sup>, C. Kopper<sup>g</sup>,  
A. Kouchner<sup>p,1</sup>, W. Kretschmer<sup>g</sup>, A. Kruijjer<sup>j</sup>, S. Kuch<sup>g</sup>, V. Kulikovskiy<sup>f,ai</sup>,  
D. Lachartre<sup>h</sup>, H. Lafoux<sup>p</sup>, P. Lagier<sup>a</sup>, R. Lahmann<sup>g</sup>,  
C. Lahonde-Hamdoun<sup>h</sup>, P. Lamare<sup>h</sup>, G. Lambard<sup>a</sup>, J.-C. Languillat<sup>h</sup>,  
G. Larosa<sup>i</sup>, J. Lavallo<sup>a</sup>, Y. Le Guen<sup>w</sup>, H. Le Provost<sup>h</sup>, A. LeVanSuu<sup>a</sup>,  
D. Lefèvre<sup>y</sup>, T. Legou<sup>a</sup>, G. Lelaizant<sup>a</sup>, C. Lévêque<sup>ab</sup>, G. Lim<sup>j,af</sup>,  
D. Lo Presti<sup>aj</sup>, H. Loehner<sup>aa</sup>, S. Loucatos<sup>p</sup>, F. Louis<sup>h</sup>, F. Lucarelli<sup>d,r</sup>,  
V. Lyashuk<sup>ak</sup>, P. Magnier<sup>h</sup>, S. Mangano<sup>b</sup>, A. Marcel<sup>h</sup>, M. Marcelin<sup>m</sup>,  
A. Margiotta<sup>n,o</sup>, J.A. Martinez-Mora<sup>i</sup>, R. Masullo<sup>r</sup>, F. Mazéas<sup>w</sup>,  
A. Mazure<sup>m</sup>, A. Meli<sup>g</sup>, M. Melissas<sup>a</sup>, E. Migneco<sup>x</sup>, M. Mongelli<sup>k</sup>,  
T. Montaruli<sup>k,al</sup>, M. Morganti<sup>q,u</sup>, L. Moscoso<sup>l,p</sup>, H. Motz<sup>g</sup>, M. Musumeci<sup>x</sup>,  
C. Naumann<sup>p</sup>, M. Naumann-Godo<sup>g,4</sup>, M. Neff<sup>g</sup>, V. Niess<sup>a</sup>,  
G.J.L. Nooren<sup>j,ah</sup>, J.E.J. Oberski<sup>j</sup>, C. Olivetto<sup>a</sup>, N. Palanque-Delabrouille<sup>p</sup>,  
D. Palioselitis<sup>j</sup>, R. Papaleo<sup>x</sup>, G.E. Pāvālaš<sup>am</sup>, K. Payet<sup>p</sup>, P. Payre<sup>a,5</sup>,  
H. Peek<sup>j</sup>, J. Petrovic<sup>j</sup>, P. Piattelli<sup>x</sup>, N. Picot-Clemente<sup>a</sup>, C. Picq<sup>p</sup>, Y. Piret<sup>h</sup>,  
J. Poinsignon<sup>h</sup>, V. Popa<sup>am</sup>, T. Pradier<sup>ad</sup>, E. Presani<sup>j</sup>, G. Prono<sup>h</sup>, C. Racca<sup>c</sup>,  
G. Raia<sup>x</sup>, J. van Randwijk<sup>j</sup>, D. Real<sup>b</sup>, C. Reed<sup>j</sup>, F. Réthoré<sup>a</sup>,  
P. Rewiersma<sup>j</sup>, G. Riccobene<sup>x</sup>, C. Richardt<sup>g</sup>, R. Richter<sup>g</sup>, J.S. Ricola<sup>a</sup>,  
V. Rigaud<sup>ab</sup>, V. Roca<sup>b</sup>, K. Roensch<sup>g</sup>, J.-F. Rolin<sup>w</sup>, A. Rostovtsev<sup>ak</sup>,  
A. Rottura<sup>f</sup>, J. Roux<sup>a</sup>, M. Rujoiu<sup>am</sup>, M. Ruppi<sup>k</sup>, G.V. Russo<sup>aj</sup>, F. Salesa<sup>b</sup>,  
K. Salomon<sup>g</sup>, P. Sapienza<sup>x</sup>, F. Schmitt<sup>g</sup>, F. Schöck<sup>g</sup>, J.-P. Schuller<sup>p,\*</sup>,  
F. Schüssler<sup>p</sup>, D. Sciliberto<sup>aj</sup>, R. Shanidze<sup>g</sup>, E. Shirokov<sup>ai</sup>, F. Simeone<sup>d</sup>,  
A. Sottoriva<sup>j,o,af</sup>, A. Spies<sup>g</sup>, T. Spona<sup>g</sup>, M. Spurio<sup>n,o</sup>, J.J.M. Steijger<sup>j</sup>,  
Th. Stolarczyk<sup>p</sup>, K. Streeb<sup>g</sup>, L. Sulak<sup>a</sup>, M. Taiuti<sup>f,an</sup>, C. Tamburini<sup>y</sup>,  
C. Tao<sup>a,p</sup>, L. Tasca<sup>m</sup>, G. Terreni<sup>q</sup>, D. Tezier<sup>a</sup>, S. Toscano<sup>b</sup>, F. Urbano<sup>b</sup>,  
P. Valdy<sup>ab</sup>, B. Vallage<sup>p</sup>, V. Van Elewyck<sup>l</sup>, G. Vannoni<sup>p</sup>, M. Vecchi<sup>a,r</sup>,  
G. Venekamp<sup>j</sup>, B. Verlaat<sup>j</sup>, P. Vernin<sup>p</sup>, E. Virique<sup>h</sup>, G. de Vries<sup>j,ah</sup>,  
R. van Wijk<sup>j</sup>, G. Wijnker<sup>j</sup>, G. Wobbe<sup>g</sup>, E. de Wolf<sup>f,af</sup>, Y. Yakovenko<sup>ai</sup>,  
H. Yepes<sup>b</sup>, D. Zaborov<sup>ak</sup>, H. Zaccone<sup>p</sup>, J.D. Zornoza<sup>b</sup>, J. Zúñiga<sup>b</sup>

<sup>a</sup>CPPM, Aix-Marseille Université, CNRS/IN2P3, Marseille, France

<sup>b</sup>IFIC - Instituto de Física Corpuscular, Edificios Investigación de Paterna, CSIC - Universitat de València, Apdo. de Correos 22085, 46071 Valencia, Spain

- <sup>c</sup>GRPHE - Institut universitaire de technologie de Colmar, 34 rue du Grillenbreit BP 50568,  
68008 Colmar, France
- <sup>d</sup>INFN - Sezione di Roma, P.le Aldo Moro 2, 00185 Roma, Italy
- <sup>e</sup>Technical University of Catalonia, Laboratory of Applied Bioacoustics, Rambla Exposició,  
08800 Vilanova i la Geltrú, Barcelona, Spain
- <sup>f</sup>INFN - Sezione di Genova, Via Dodecaneso 33, 16146 Genova, Italy
- <sup>g</sup>Friedrich-Alexander-Universität Erlangen-Nürnberg, Erlangen Centre for Astroparticle Physics,  
Erwin-Rommel-Str. 1, 91058 Erlangen, Germany
- <sup>h</sup>Direction des Sciences de la Matière - Institut de recherche sur les lois fondamentales de l'Univers -  
Service d'Electronique des Détecteurs et d'Informatique, CEA Saclay,  
91191 Gif-sur-Yvette Cedex, France
- <sup>i</sup>Institut d'Investigació per a la Gestió Integrada de Zones Costaneres (IGIC) - Universitat Politècnica  
de València. C/ Paranímf 1. , 46730 Gandia, Spain.
- <sup>j</sup>Nikhef, Science Park, Amsterdam, The Netherlands
- <sup>k</sup>INFN - Sezione di Bari, Via E. Orabona 4, 70126 Bari, Italy
- <sup>l</sup>APC - Laboratoire AstroParticule et Cosmologie, UMR 7164 (CNRS, Université Paris 7 Diderot,  
CEA, Observatoire de Paris), 10 rue Alice Domon et Léonie Duquet, 75205 Paris Cedex 13, France
- <sup>m</sup>LAM - Laboratoire d'Astrophysique de Marseille, Pôle de l'Étoile Site de Château-Gombert,  
rue Frédéric Joliot-Curie 38, 13388 Marseille Cedex 13, France
- <sup>n</sup>Dipartimento di Fisica dell'Università, Viale Berti Pichat 6/2, 40127 Bologna, Italy
- <sup>o</sup>INFN - Sezione di Bologna, Viale Berti Pichat 6/2, 40127 Bologna, Italy
- <sup>p</sup>Direction des Sciences de la Matière - Institut de recherche sur les lois fondamentales de l'Univers -  
Service de Physique des Particules, CEA Saclay, 91191 Gif-sur-Yvette Cedex, France
- <sup>q</sup>INFN - Sezione di Pisa, Largo B. Pontecorvo 3, 56127 Pisa, Italy
- <sup>r</sup>Dipartimento di Fisica dell'Università La Sapienza, P.le Aldo Moro 2, 00185 Roma, Italy
- <sup>s</sup>INFN - Sezione di Catania, Viale Andrea Doria 6, 95125 Catania, Italy
- <sup>t</sup>Laboratoire de Physique Corpusculaire, IN2P3-CNRS, Université Blaise Pascal,  
Clermont-Ferrand, France
- <sup>u</sup>Dipartimento di Fisica dell'Università, Largo B. Pontecorvo 3, 56127 Pisa, Italy
- <sup>v</sup>Géoazur - Université de Nice Sophia-Antipolis, CNRS/INSU, IRD, Observatoire de la Côte d'Azur et  
Université Pierre et Marie Curie, BP 48, 06235 Villefranche-sur-mer, France
- <sup>w</sup>IFREMER - Centre de Brest, BP 70, 29280 Plouzané, France
- <sup>x</sup>INFN - Laboratori Nazionali del Sud (LNS), Via S. Sofia 62, 95123 Catania, Italy
- <sup>y</sup>COM - Centre d'Océanologie de Marseille, CNRS/INSU et Université de la Méditerranée,  
163 Avenue de Luminy, Case 901, 13288 Marseille Cedex 9, France
- <sup>z</sup>Université Paris-Sud , 91405 Orsay Cedex, France
- <sup>aa</sup>Kernfysisch Versneller Instituut (KVI), University of Groningen, Zernikelaan 25,  
9747 AA Groningen, The Netherlands
- <sup>ab</sup>IFREMER - Centre de Toulon/La Seyne Sur Mer, Port Brégaillon, Chemin Jean-Marie Fritz,  
83500 La Seyne sur Mer, France
- <sup>ac</sup>Direction des Sciences de la Matière - Institut de recherche sur les lois fondamentales de l'Univers -  
Service d'Astrophysique, CEA Saclay, 91191 Gif-sur-Yvette Cedex, France
- <sup>ad</sup>IPHC-Institut Pluridisciplinaire Hubert Curien - Université de Strasbourg et CNRS/IN2P3,  
23 rue du Loess, BP 28, 67037 Strasbourg Cedex 2, France
- <sup>ae</sup>Royal Netherlands Institute for Sea Research (NIOZ), Landsdiep 4,  
1797 SZ 't Horntje (Texel), The Netherlands
- <sup>af</sup>Universiteit van Amsterdam, Instituut voor Hoge-Energiefysika, Science Park 105,  
1098 XG Amsterdam, The Netherlands
- <sup>ag</sup>Dr. Remeis-Sternwarte Bamberg, Sternwartstrasse 7, 96049 Bamberg, Germany
- <sup>ah</sup>Universiteit Utrecht, Faculteit Betawetenschappen, Princetonplein 5,  
3584 CC Utrecht, The Netherlands
- <sup>ai</sup>Moscow State University, Skobel'syn Institute of Nuclear Physics, Leninskies gory,  
119991 Moscow, Russia
- <sup>aj</sup>Dipartimento di Fisica ed Astronomia dell'Università, Viale Andrea Doria 6, 95125 Catania, Italy
- <sup>ak</sup>ITEP - Institute for Theoretical and Experimental Physics, B. Chermushkinskaya 25,  
117218 Moscow, Russia
- <sup>al</sup>University of Wisconsin - Madison, 53715, WI, USA

## Abstract

The ANTARES Neutrino Telescope was completed in May 2008 and is the first operational Neutrino Telescope in the Mediterranean Sea. The main purpose of the detector is to perform neutrino astronomy and the apparatus also offers facilities for marine and Earth sciences. This paper describes the design, the construction and the installation of the telescope in the deep sea, offshore from Toulon in France. An illustration of the detector performance is given.

*Keywords:* neutrino, astroparticle, neutrino astronomy, deep sea detector, marine technology, DWDM, photomultiplier tube, submarine cable, wet mateable connector.

---

1	<b>Contents</b>	
2	<b>1 Introduction</b>	<b>9</b>
3	<b>2 Basic concepts</b>	<b>11</b>
4	2.1 Detection principle . . . . .	11
5	2.2 General description of the detector . . . . .	11
6	2.2.1 Detector layout . . . . .	11
7	2.2.2 Detector architecture . . . . .	12
8	2.2.3 Master clock system . . . . .	14
9	2.2.4 Positioning system . . . . .	15
10	2.2.5 Timing calibration systems . . . . .	16
11	2.3 Detector design considerations . . . . .	16
12	<b>3 Line structure</b>	<b>18</b>
13	3.1 Optical modules . . . . .	18
14	3.1.1 Photo detector requirements . . . . .	19
15	3.1.2 Optical module components . . . . .	19
16	3.1.2.1 Photomultiplier tube . . . . .	19
17	3.1.2.2 Glass sphere . . . . .	21

18	3.1.2.3	Optical gel . . . . .	22
19	3.1.2.4	Magnetic shield . . . . .	22
20	3.1.2.5	HV power supply . . . . .	23
21	3.1.2.6	Internal LED . . . . .	23
22	3.1.2.7	Link with the electronics container . . . . .	24
23	3.1.2.8	Final assembly and tests . . . . .	24
24	3.1.3	OM support . . . . .	25
25	3.2	Storey . . . . .	26
26	3.2.1	Optical module frame . . . . .	26
27	3.2.2	Local control module . . . . .	27
28	3.2.2.1	Container . . . . .	27
29	3.2.2.2	Electronics . . . . .	28
30	3.3	Electro-optical mechanical cable (EMC) . . . . .	32
31	3.4	Bottom string structure . . . . .	36
32	3.4.1	Dead weight . . . . .	36
33	3.4.2	Release system . . . . .	37
34	3.4.3	Recoverable part . . . . .	37
35	3.5	Top buoy . . . . .	39
36	3.6	Mechanical behaviour of a line . . . . .	40
37	3.7	Timing calibration devices . . . . .	41
38	3.7.1	LED beacons . . . . .	41
39	3.7.2	Laser beacons . . . . .	43
40	3.8	Positioning devices . . . . .	44
41	3.9	Instrumentation line . . . . .	45
42	3.10	Acoustic detection system AMADEUS . . . . .	46
43	<b>4</b>	<b>Detector infrastructure</b>	<b>47</b>
44	4.1	Interlink cable . . . . .	47
45	4.2	Junction box . . . . .	48
46	4.2.1	Junction box mechanical layout . . . . .	48
47	4.2.2	Junction box cabling . . . . .	49
48	4.2.3	Junction box slow control electronics . . . . .	50
49	4.2.4	Fibre optic signal distribution in the junction box . . . . .	52
50	4.3	Main electro-optical cable . . . . .	53
51	4.3.1	Cable . . . . .	53
52	4.3.2	Power supply to the junction box . . . . .	55
53	4.4	Shore facilities . . . . .	56

54	<b>5 Construction</b>	<b>57</b>
55	5.1 Generalities . . . . .	57
56	5.2 Quality assurance and quality control . . . . .	58
57	5.3 Assembly . . . . .	59
58	5.3.1 Control module integration . . . . .	59
59	5.3.2 Line integration . . . . .	59
60	5.3.3 Deployment preparation . . . . .	59
61	5.4 Line deployments and connections . . . . .	60
62	5.5 Maintenance . . . . .	61
63	<b>6 Operation</b>	<b>62</b>
64	6.1 Apparatus control . . . . .	62
65	6.2 Data acquisition . . . . .	63
66	6.3 Trigger . . . . .	64
67	6.4 Calibration . . . . .	66
68	6.4.1 Position determination . . . . .	66
69	6.4.2 Timing calibration . . . . .	69
70	6.4.3 Amplitude calibration . . . . .	72
71	6.5 Performance of the apparatus . . . . .	74
72	<b>7 Conclusions</b>	<b>78</b>

73	<b>Acronyms and abbreviations</b>
74	<b>ADCP</b> Acoustic Doppler Current Profiler
75	<b>ARS</b> Analogue Ring Sampler
76	<b>AS</b> Acoustic Storey
77	<b>AVC</b> Amplitude to Voltage Converter
78	<b>BSS</b> Bottom String Socket
79	<b>CTD</b> Conductivity Temperature Depth sensor
80	<b>DAQ</b> Data Acquisition
81	<b>DP</b> Dynamic Positioning
82	<b>DSP</b> Digital Signal Processor
83	<b>DWDM</b> Dense Wavelength Division Multiplexer
84	<b>EMC</b> (vertical) Electro Mechanical Cable
85	<b>GCN</b> Gamma-ray bursts Coordinates Network
86	<b>GUI</b> Graphical User Interface
87	<b>HFLBL</b> High Frequency Long Base Line
88	<b>ID</b> Inner Diameter
89	<b>IL</b> InterLink
90	<b>IL07</b> Instrumented Line (deployed in the year 2007)
91	<b>JB</b> Junction Box
92	<b>LCM</b> Local Control Module
93	<b>LDPE</b> Low Density PolyEthylene
94	<b>LFLBL</b> Low Frequency Long Base Line
95	<b>LPB</b> Local Power Box
96	<b>LQS</b> Local Quality Supervisor
97	<b>MEOC</b> Main Electro Optical Cable
98	<b>MLCM</b> Master Local Control Modul
99	<b>NWB</b> Non-Water-Blocking
100	<b>OD</b> Outer Diameter
101	<b>OM</b> Optical Module
102	<b>OMF</b> Optical Module Frame

103	<b>PBS</b> Product Breakdown Structure
104	<b>PETP</b> PolyEthylene TerePhthalate
105	<b>PMT</b> Photo Multiplier Tube
106	<b>PU</b> PolyUrethane
107	<b>QA/QC</b> Quality Assurance / Quality Control
108	<b>ROV</b> Remote Operated Vehicle
109	<b>SC</b> Slow Control
110	<b>SCM</b> String Control Module
111	<b>SPE</b> Single Photo Electron
112	<b>SPM</b> String Power Module
113	<b>SV</b> Sound Velocimeter
114	<b>TS</b> TimeStamp
115	<b>TVC</b> Time to Voltage Converter
116	<b>TTS</b> Transit Time Spread
117	<b>VNC</b> Virtual Network Computing
118	<b>WB</b> Water-Blocking
119	<b>WDM</b> Wavelength Division Multiplexer
120	<b>WF</b> WaveForm sampling



## 121 1. Introduction

122 Neutrino Astronomy is a new and unique method to observe the Universe.  
123 The weakly interacting nature of the neutrino make it a complementary cos-  
124 mic probe to other messengers such as multi-wavelength light and charged  
125 cosmic rays: the neutrino can escape from sources surrounded with dense  
126 matter or radiation fields and can travel cosmological distances without being  
127 absorbed. This specificity of the neutrino astronomy means that in addition  
128 to knowledge on cosmic accelerators seen by other messengers, it may lead to  
129 the discovery of objects hitherto unknown. For known high energy sources  
130 such as active galactic nuclei, gamma ray bursters, microquasars and super-  
131 nova remnants, neutrinos will allow to distinguish unambiguously between  
132 hadronic and electronic acceleration mechanisms and to localize the acceler-  
133 ation sites more precisely than charged cosmic ray detectors. The ability of  
134 neutrinos to exit dense sources means that new compact acceleration sites  
135 might be discovered. Furthermore, this feature gives an exclusive signal for  
136 indirect searches of dark matter based on the detection of high energy prod-  
137 ucts from the annihilation of dark matter particles which might have been  
138 accumulated in the cores of dense objects such as the Sun, Earth and the  
139 centre of the Galaxy. Although the search for a diffuse flux of neutrinos from  
140 unresolved distant sources is in the research program of neutrino telescopes,  
141 the main emphasis of the program is to search for distinct point sources of  
142 neutrinos such as the examples mentioned above. In this matter, the angu-  
143 lar resolution of the neutrino telescope is of particular importance: not only  
144 to resolve and correlate sources with other instruments using other messen-  
145 gers, but also because it plays an important role in rejecting background.  
146 The flux of neutrinos from interactions of cosmic rays with the atmosphere  
147 (“atmospheric neutrinos”) is an irreducible source of background which only  
148 differs from the neutrino signal from distant objects in the energy spectrum.  
149 To distinguish a signal from point sources in this background, good angu-  
150 lar resolution greatly improves the telescope sensitivity. At a given energy,  
151 this angular resolution depends on the optical scattering properties of the  
152 medium and on the size of the detector.

153 The ANTARES detector, located 40 km offshore from Toulon at 2475  
154 m depth<sup>6</sup>, was completed on 29 May 2008, making it the largest neutrino  
155 telescope in the northern hemisphere and the first to operate in the deep sea.

---

<sup>6</sup>42°48N, 6°10E

156 The technological developments made for ANTARES have extensively been  
157 built on the experience of the pioneer DUMAND project [1] as well as the  
158 operational BAIKAL [2] detector in Siberia. Some features of the ANTARES  
159 design are common with the AMANDA/ICECUBE [3] detector at the South  
160 Pole.

161 The detector infrastructure has 12 mooring lines holding light sensors de-  
162 signed for the measurement of neutrino induced charged particles based on  
163 the detection of Cherenkov light emitted in water. The ANTARES telescope  
164 extends in a significant way the reach of neutrino astronomy in a complemen-  
165 tary region of the Universe to the South Pole experiments, in particular the  
166 central region of the local galaxy. Furthermore, due to its location in the deep  
167 sea, the infrastructure provides opportunities for innovative measurements in  
168 Earth and sea sciences. An essential attribute of the infrastructure is the per-  
169 manent connection to shore with the capacity for high-bandwidth acquisition  
170 of data, providing the opportunity to install sensors for sea parameters giving  
171 continuous long-term measurements. Instruments for research in marine and  
172 Earth sciences are distributed on the 12 optical lines of the detector and are  
173 also located on a 13<sup>th</sup> line specifically dedicated to the monitoring of the sea  
174 environment.

175 Another project benefiting from the deep sea infrastructure is an R&D  
176 system of hydrophones which investigates the detection of ultra-high energy  
177 neutrinos using the sound produced by their interaction in water. This sys-  
178 tem called AMADEUS (Antares Modules for the Acoustic Detection Under  
179 the Sea) is a feasibility study for a prospective future large scale acoustic  
180 detector. This technique aims to detect neutrinos with energies exceeding  
181 100 PeV. The advantage of the acoustic technique is the attenuation length  
182 which is about 5 km for the peak spectral density of the generated sound  
183 waves around 10 kHz while the attenuation of Cherenkov light in water is  
184 about 60 m.

185 This paper describes the design, construction and operation of the AN-  
186 TARES Neutrino Telescope with emphasis on the aspects of the infrastruc-  
187 ture important for neutrino astronomy. The scope of the present paper is  
188 to describe the detector as it was built, the extensive experience obtained in  
189 developing this technology will be described in other documents. The marine  
190 and Earth sciences aspects of the project are described in other places [4, 5, 6]  
191 as is the AMADEUS acoustic detection system [7].

192 Following a summary of the basic concepts of the neutrino detection tech-  
193 nique and of the detector architecture, the detector elements are described.

194 For some aspects of the detector separate papers have been published and  
195 for these the present paper will give a short overview with appropriate refer-  
196 ences. Those features of the detector which are not described elsewhere are  
197 covered in more details. Finally, this paper summarizes the construction and  
198 sea deployment of the detector and ends with a description of the detector  
199 operation including some performance characteristics.

## 200 **2. Basic concepts**

### 201 *2.1. Detection principle*

202 The telescope is optimised to detect upward going high energy neutri-  
203 nos by observing the Cherenkov light produced in sea water from secondary  
204 charged leptons which originate in charged current interactions of the neutri-  
205 nos with the matter around the instrumented volume. Due to the long range  
206 of the muon, neutrino interaction vertices tens of kilometres away from the  
207 detector can be observed. Other neutrino flavours are also detected, though  
208 with lower efficiency and worse angular precision because of the shorter range  
209 of the corresponding leptons. In the following the description of the detection  
210 principle will concentrate on the muon channel.

211 To detect the Cherenkov light, the neutrino telescope comprises a ma-  
212 trix of light detectors, in the form of photomultipliers contained in glass  
213 spheres, called Optical Modules (OM), positioned on flexible lines anchored  
214 to the seabed. The muon track is reconstructed using the measurements of  
215 the arrival times of the Cherenkov photons on the OMs of known positions.  
216 With the chosen detector dimensions, the ANTARES detector has a low  
217 energy threshold of about 20 GeV for well reconstructed muons. The Monte-  
218 Carlo simulations indicate that the direction of the incoming neutrino, almost  
219 collinear with the secondary muon at high energy, can be determined with  
220 an accuracy better than  $0.3^\circ$  for energies above 10 TeV. Figure 1 illustrates  
221 the principle of neutrino detection with the undersea telescope.

### 222 *2.2. General description of the detector*

#### 223 *2.2.1. Detector layout*

224 The basic detection element is the optical module housing a photomulti-  
225 plier tube (PMT). The nodes of the three-dimensional telescope matrix are  
226 called storeys. Each storey is the assembly of a mechanical structure, the  
227 Optical Module Frame (OMF), which supports three OMs, looking down-  
228 wards at  $45^\circ$ , and a titanium container, the Local Control Module (LCM),

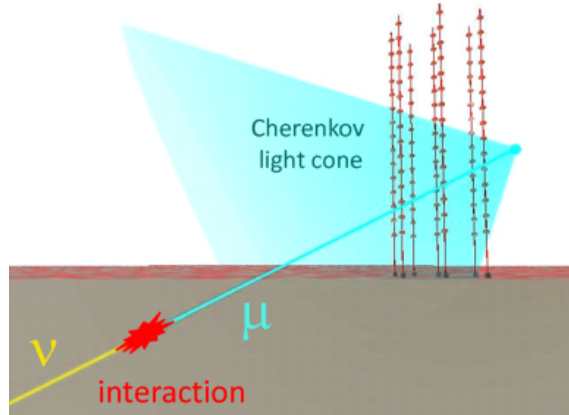


Figure 1: Principle of detection of high energy muon neutrinos in an underwater neutrino telescope. The incoming neutrino interacts with the material around the detector to create a muon. The muon gives Cherenkov light in the sea water which is then detected by a matrix of light sensors. The original spectrum of light emitted from the muon is attenuated in the water such that the dominant wavelength range detected is between 350 and 500 nm.

229 housing the offshore electronics and embedded processors. In its nominal  
 230 configuration, a detector line is formed by a chain of 25 OMFs linked with  
 231 Electro-Mechanical Cable segments (EMC). The distance is 14.5 m between  
 232 storeys and 100 m from the seabed to the first storey. The line is anchored  
 233 on the seabed with the Bottom String Socket (BSS) and is held vertical by a  
 234 buoy at the top. The full neutrino telescope comprises 12 lines, 11 with the  
 235 nominal configuration, the twelfth line being equipped with 20 storeys and  
 236 completed by devices dedicated to acoustic detection (Section 3.10). Thus,  
 237 the total number of the OMs installed in the detector is 885. The lines are  
 238 arranged on the seabed in an octagonal configuration and is illustrated in  
 239 Figure 2. It is completed by the Instrumentation Line (IL07) which sup-  
 240 ports the instruments used to perform environmental measurements. The  
 241 data communication and the power distribution to the lines are done via  
 242 an infrastructure on the seabed which consists of Inter Link cables (IL), the  
 243 Junction Box (JB) and the Main Electro-Optical Cable (MEOC).

#### 244 2.2.2. Detector architecture

245 The Data Acquisition system (DAQ) is based on the “all-data-to-shore”  
 246 concept [8]. In this mode, all signals from the PMTs that pass a preset  
 247 threshold (typically 0.3 Single Photo Electron (SPE)) are digitized in a cus-

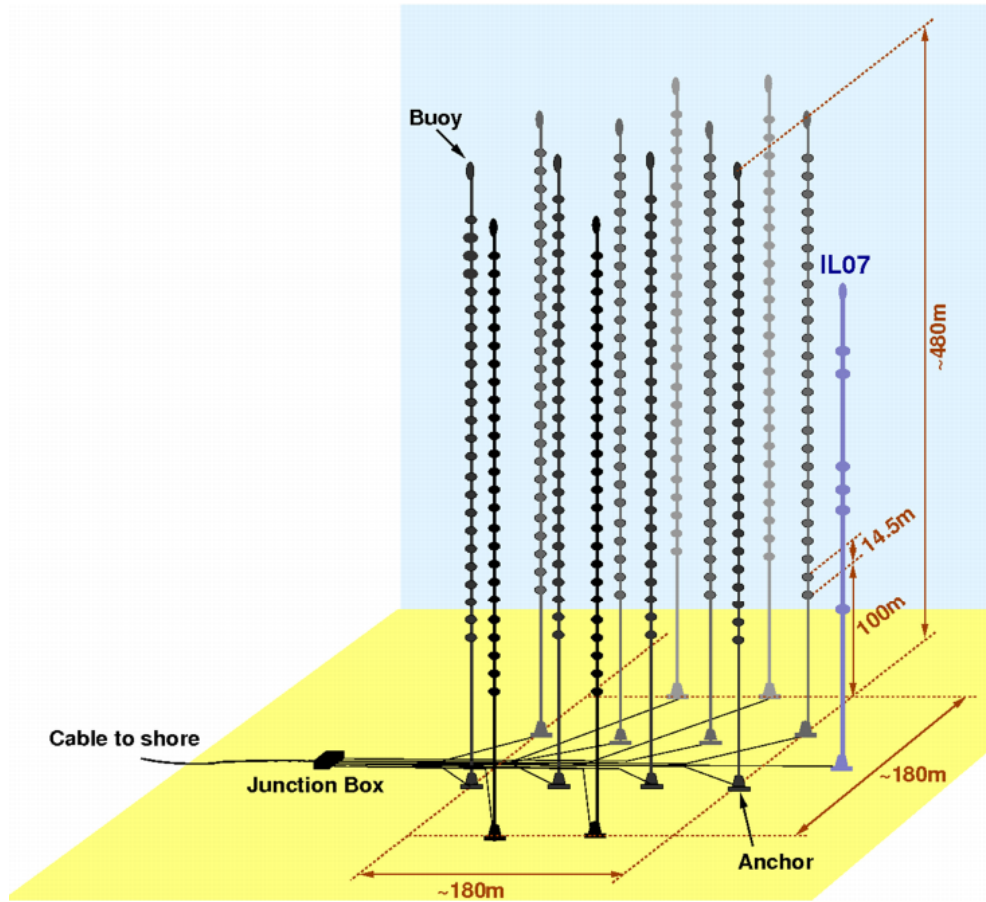


Figure 2: Schematic view of the ANTARES detector.

248 tom built ASIC chip, the Analogue Ring Sampler (ARS) [9], and all digital  
 249 data are sent to shore where they are processed in real-time by a farm of  
 250 commodity PCs. The data flow ranges from a couple of  $\text{Gb s}^{-1}$  to several  
 251 tens of  $\text{Gb s}^{-1}$ , depending on the level of the submarine bioluminescent activity.  
 252 To cope with this large amount of data, the readout architecture of the  
 253 detector has a star topology with several levels of multiplexing. The first  
 254 level is in the LCM of each storey of the detector, where the data acquisition  
 255 card containing an FPGA and a microprocessor outputs the digitised data of  
 256 the three optical modules. The card is also equipped with dedicated memory  
 257 to allow local data storage and it manages the delayed transmission of data  
 258 in order to avoid network congestion. The transmission is done through a

259 bi-directional optical fibre to the Master Local Control Module (MLCM),  
260 a specific LCM located every fifth storey. It is equipped with an Ethernet  
261 switch which gathers the data from the local OMs and from the four con-  
262 nected storeys. Such a group of 5 storeys is called a sector. The switch of  
263 each sector is connected via a pair of uni-directional fibres to a Dense Wave-  
264 length Division Multiplexing (DWDM) system in an electronics container,  
265 the String Control Module (SCM), situated on the BSS at the bottom of  
266 each line. The DWDM system is then connected to the junction box on the  
267 seabed via the interlink cables. In the junction box the outputs from up to  
268 16 lines are gathered onto the MEOC and sent to the shore station. In the  
269 shore station, the data are demultiplexed and treated by a PC farm where  
270 they are filtered and then sent via the commercial fibre optic network to be  
271 stored remotely at a computer centre in Lyon<sup>7</sup>. A schematic view of the  
272 readout architecture is shown in Figure 3.

273 The electrical supply system has a similar architecture to the readout sys-  
274 tem. The submarine cable supplies up to 4400 VAC, 10 A to a transformer  
275 in the junction box. The sixteen independent secondary outputs from the  
276 transformer provide up to 500 VAC, 4 A to the lines via the interlink cables.  
277 At the base of each line a String Power Module (SPM) power supply dis-  
278 tributes up to 400 VDC to each sector. The MLCM and LCMs of the sector  
279 are fed in parallel and the power is used by a Local Power Box (LPB) in  
280 each storey to provide the various low voltages required by each electronics  
281 board.

### 282 *2.2.3. Master clock system*

283 Precise timing resolution for the recorded PMT signals, of order 1 ns, is  
284 required to maintain the angular resolution of the telescope. An essential  
285 element to achieve this precision is a 20 MHz master clock system, based  
286 onshore, which delivers a common reference time to all the offshore electronics  
287 in the LCMs. This system delivers a timestamp, derived from GPS time, via  
288 a fibre optic network from the shore station to the junction box and then  
289 to each line base and each LCM. The master clock system is self calibrating  
290 and periodically measures the time path from shore to the LCM by echoing  
291 signals received in the LCM back to the shore station.

---

<sup>7</sup><http://cc.in2p3.fr>

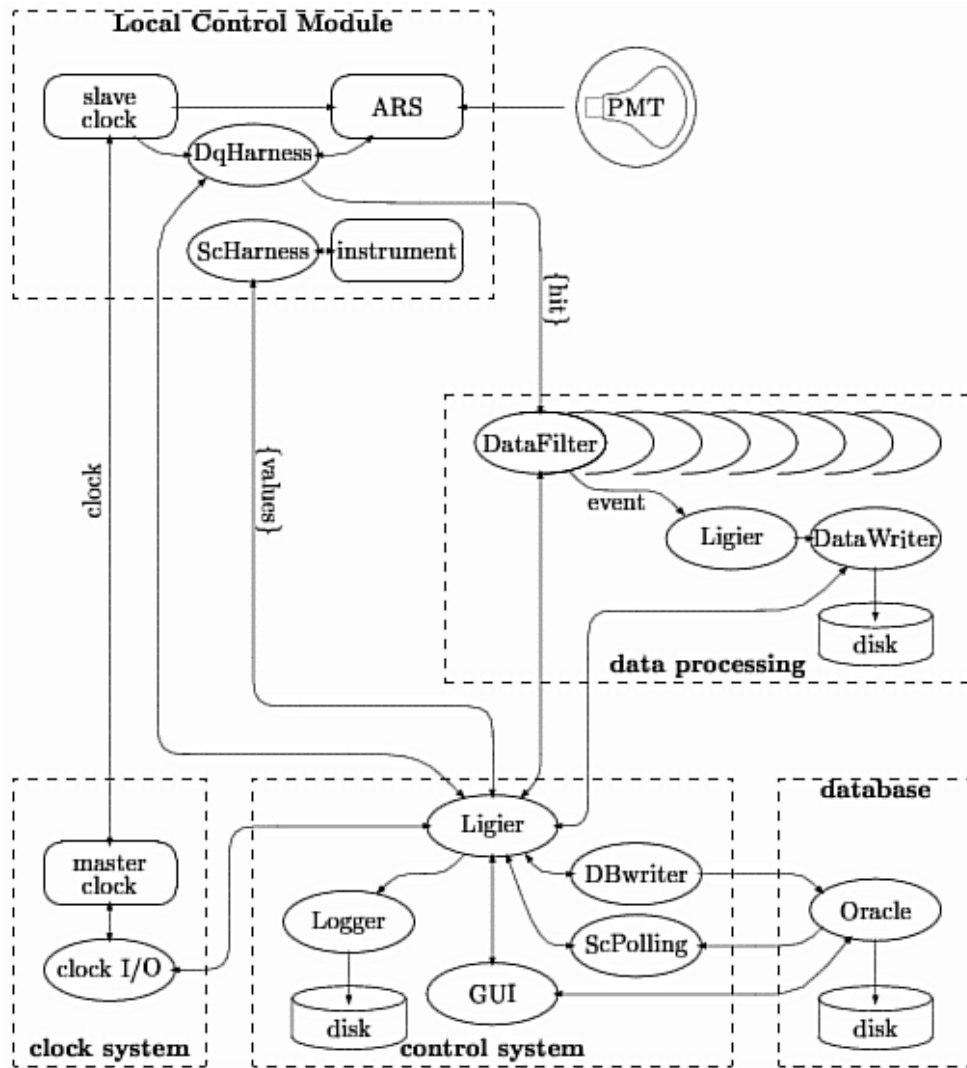


Figure 3: Schematic view of the data acquisition system. The dashed line boxes refer to hardware devices, the ellipses correspond to processes running on those devices. The lines between processes indicate the exchange of information (commands, data, messages, etc.).

292 *2.2.4. Positioning system*

293 The detector lines connecting the OMs are flexible and are moving con-  
 294 tinually in the sea current. In order to ensure optimal track reconstruction  
 295 accuracy, it is necessary to monitor the relative positions of all OMs with

296 accuracy better than 20 cm, equivalent to the 1 ns precision of the timing  
297 measurements. The reconstruction of the muon trajectory and the determi-  
298 nation of its energy also require the knowledge of the OM orientation with a  
299 precision of a few degrees. In addition, a precise absolute orientation of the  
300 whole detector has to be achieved in order to find potential neutrino point-  
301 sources in the sky. To attain a suitable precision on the overall positioning  
302 accuracy, a constant monitoring with two independent systems is used:

- 303 • A High Frequency Long Base Line acoustic system (HFLBL) giving  
304 the 3D position of hydrophones placed along the line. These positions  
305 are obtained by triangulation from emitters anchored in the base of the  
306 line plus autonomous transponders on the sea floor.
- 307 • A set of tiltmeter-compass sensors giving the local tilt angles of each  
308 storey with respect to the vertical line (pitch and roll) as well as its  
309 orientation with respect to the Earth magnetic north (heading).

#### 310 *2.2.5. Timing calibration systems*

311 The timing calibration of the detector was performed during the construc-  
312 tion and is continually verified and adjusted during operation on a weekly  
313 basis. The master clock system measures the time delays between the shore  
314 station and the LCMs leaving only the short delays between the electronics  
315 in the LCM and the photon arrival at the PMT photocathode as a time  
316 offset requiring further calibration. These offsets are first measured after  
317 line assembly on shore and then again in the sea after deployment. This  
318 *in situ* calibration uses a system of external light sources (optical beacons)  
319 distributed throughout the detector. There are two types of optical beacons:  
320 LED beacons located in four positions on each detector line and laser beacons  
321 located on the bottom of two particular lines. In addition, there is an LED  
322 inside each optical module which is used to monitor changes in the transit  
323 time of the photomultiplier.

#### 324 *2.3. Detector design considerations*

325 The detector location on the seabed at a depth of 2475 m imposes many  
326 constraints on the detector design. All components must withstand a hydro-  
327 static pressure between 200 and 256 bar and resist corrosion or degradation  
328 in the sea water of 46 mS cm<sup>-1</sup> conductivity. The seabed environment has  
329 a stable temperature around 13 °C and little risk of shock or variable me-  
330chanical stress. The detector lines sway in the sea current which is typically



331 10 cm s<sup>-1</sup> with variations up to a maximum value of 30 cm s<sup>-1</sup>. The detector  
332 components were designed to take into account possible shocks, vibrations  
333 and high temperatures during construction, transport and deployment. All  
334 components were chosen with the objective of a minimum detector life time  
335 of 10 years.

336 The materials to be in contact with the sea water were selected accord-  
337 ing to their known resistance to corrosion: glass, titanium alloys (grade  
338 2 and 5), anode protected carbon steel, polyethylene (LDPE and PETP),  
339 polyurethane, aramid and glass-epoxy (syntactic foam and fibre composite).  
340 Stainless steel and aluminium alloys were not used due to their reduced cor-  
341 rosion resistance. In addition to this material selection, special attention was  
342 paid to prevent any parasitic electrical currents able to induce electrolytic  
343 corrosion. Isolating interfaces were used between metals of different nature  
344 and the electrical power distribution system was designed to prevent any  
345 current leak to the water.

346 Avoiding water leaks during operation imposed many constraints on the  
347 detector design. When possible, O-rings in containers, made of Viton<sup>8</sup> or  
348 nitrile material were implemented in two seals in a redundant way. The  
349 O-ring material hardness, its cross section diameter, the shape and the sur-  
350 face roughness of the groove as well as the characteristics of the matching  
351 parts were specified following the recommendations of the manufacturer for  
352 the *in situ* pressure. Tests under pressure were performed on all the major  
353 containers (JB container and glass spheres) and EMC sections. Electron-  
354 ics containers have been tested by sampling. Some tests were performed by  
355 the manufacturer of the component (glass spheres and short sections of the  
356 EMC ) and others were performed by the collaboration at IFREMER<sup>9</sup>, at  
357 the COMEX<sup>10</sup> and Ring-O Valve<sup>11</sup> companies (JB and electronics contain-  
358 ers, the rest of the EMC sections). The pressure tests were based on the  
359 IFREMER rules for undersea vessels for a working pressure of 256 bar: a  
360 cycle up to 310 bar for 24 h and ten cycles up to 256 bar for 1h with all the  
361 pressure changes made at a rate of  $\pm 12$  bar per minute. The criterion of  
362 success for the acceptance test was the integrity of the tested element, the  
363 absence of water inside the containers and the electro-optical continuity of

---

<sup>8</sup>Viton®, <http://www.dupontelastomers.com/products/viton/>

<sup>9</sup>IFREMER, [www.ifremer.fr](http://www.ifremer.fr)

<sup>10</sup>COMEX, [www.comex.fr](http://www.comex.fr)

<sup>11</sup>Ring-O Valve SpA, 23823 Colico, Italy.

364 the cable under static pressure conditions.

365 The maximum static tension along the line is expected to occur during  
366 the line deployment in the section below the first storey, which has to sustain  
367 the weight in water of the full anchor (BSS + deadweight):  $\approx 3$  tons. Dy-  
368 namic load may reach higher values during the deployment, due to the swell.  
369 Since the total mass of the line is 7 tons, an upward acceleration of 1  $g$ , for  
370 instance, will add a tension of 70 kN in the top part of the line during the  
371 descent. In order to minimise the risks of high dynamic loads, the deploy-  
372 ment of the lines were required to be performed in quiet sea state ( $\leq 3$  on  
373 the Beaufort scale, corresponding to waves of  $\approx 60$  cm high). However, since  
374 the conditions are difficult to predict accurately for the  $\approx 8$  hours needed for  
375 a deployment or a recovery, the general dimensioning rules recommended by  
376 IFREMER for deployments in the sea from a surface boat were imposed:

$$\textit{Breaking Load} > \textit{Static Load} \times A \quad (1)$$

377 where  $A = 1.5$  for metal parts (BSS, OMF and buoy equipment) and 4 for  
378 organic fibres (the Aramid braid of the vertical EMC). This rule results in a  
379 breaking load of more than 7 tons for the OMF and 18 tons for the EMC.

### 380 **3. Line structure**

381 A line is the assembly of an anchor sitting on the seabed, 25 storeys and  
382 a top buoy linked by electro-optical mechanical cables. A storey consists of  
383 three optical modules, the metal structure that supports them and provides  
384 interfaces with the EMCs, the electronics container and additional instru-  
385 mentation. In order to limit the number of single point failures for a full  
386 line, a line is divided in 5 sectors of 5 successive storeys each. The sectors  
387 are independent for the power distribution and the data transmission. The  
388 distribution of power and routing of clock and acquisition signals toward each  
389 sector are performed in electronics containers fixed on the BSS.

#### 390 *3.1. Optical modules*

391 The optical module, the basic sensor element of the telescope, is the  
392 assembly of a pressure resistant glass sphere housing a photomultiplier tube,  
393 its base and other components. A detailed description of the ANTARES OM  
394 can be found in [10].

395 *3.1.1. Photo detector requirements*

396 The search for a highly sensitive light detector led to the choice of pho-  
397 tomultiplier tubes with a photocathode area as large as possible combined  
398 with a large angular acceptance. Regarding these criteria, the best candi-  
399 dates are large hemispherical tubes. However, the PMT size is limited by  
400 some characteristics which increase with the photocathode area:

- 401 - the transit time spread (TTS) which has to be small enough to ensure  
402 the required time resolution,
- 403 - the dark count rate which must be negligible compared to photon back-  
404 ground rate.

405 In summary, the main requirements for the choice of the ANTARES  
406 PMTs are:

- 407 ○ photocathode area  $> 500 \text{ cm}^2$
- 408 ○ quantum efficiency  $> 20 \%$
- 409 ○ collection efficiency  $> 80\%$
- 410 ○ TTS  $< 3 \text{ ns}$
- 411 ○ dark count rate  $< 10 \text{ kHz}$  (threshold at 1/3 SPE, including glass  
412 sphere)
- 413 ○ peak/valley ratio  $> 2$
- 414 ○ peak width (FWHM)/peak position  $< 50\%$
- 415 ○ gain of  $5 \times 10^7$  reached with HV  $< 2000 \text{ V}$
- 416 ○ pre-pulse rate  $< 1\%$
- 417 ○ after-pulse rate  $< 15\%$

418 *3.1.2. Optical module components*

419 Figure 4 shows a schematic view of an optical module with its main  
420 components. The following sections describe the different components and,  
421 when relevant, the assembly process.

422 *3.1.2.1. Photomultiplier tube.*

423 In the R&D phase, an extensive series of tests were performed on several  
424 commercially available models of large hemispherical photomultipliers. A  
425 summary of this study is presented in [11]. The R7081-20, a 10" hemispheri-  
426 cal tube from Hamamatsu<sup>12</sup>, was chosen. The full sample of delivered PMTs  
427 has been tested with a dedicated test bench in order to calibrate the sensors  
428 and to check the compliance with the specifications. The number of rejected

---

<sup>12</sup>Hamamatsu Photonics, Electron tube division, <http://www.hamamatsu.com>

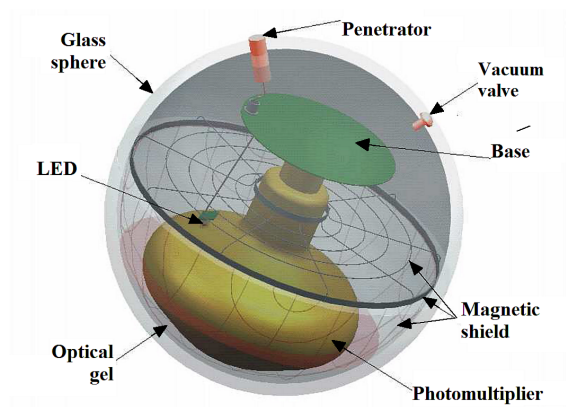


Figure 4: Schematic view of an optical module

429 tubes was small (17, their peak/valley ratio being too low), these tubes were  
 430 replaced by the manufacturer. To illustrate the homogeneity of the produc-  
 431 tion, Figure 5 shows the measured values of dark noise rate (top) and of the  
 peak/valley ratio (bottom). During the testing process, the working point of

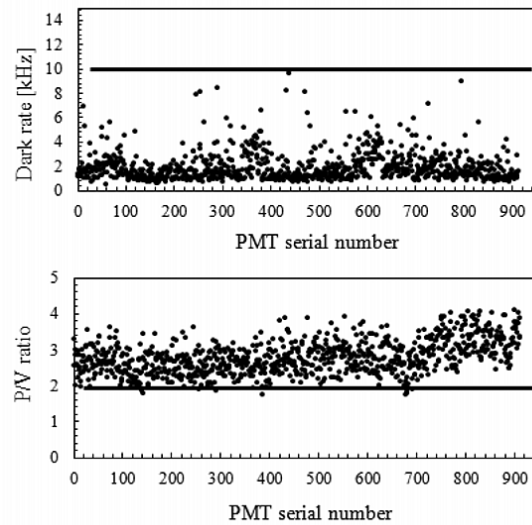


Figure 5: Results of dark count rate (top) and peak/valley ratio (bottom) for the full set of tested PMTs.

432 each PMT, i.e. the high voltage needed to obtain a gain of  $5 \times 10^7 \pm 10 \%$ ,  
 433 was determined by measuring the value of the SPE pulse height. The results  
 434

of these measurements are illustrated in Figure 6.

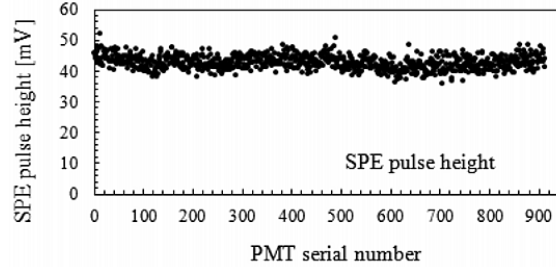


Figure 6: Measured mean pulse height of single photoelectrons for each PMT at nominal gain.

435

436 *3.1.2.2. Glass sphere.*

437 The protective envelope of the PMT is a glass sphere of a type rou-  
 438 tinely used by sea scientists for buoyancy and for instrument housing. These  
 439 spheres, because of their mechanical resistance to a compressive stress and of  
 440 their transparency, provide a convenient housing for the photodetectors. Ta-  
 441 ble 1 summarizes the main characteristics of the Vitrovex<sup>®</sup> glass spheres<sup>13</sup>  
 used. The sphere is provided as two hemispheres: one, referred to as “back

Outer diameter	432 mm (17")
Wall thickness	15 mm
Type of glass	Borosilicate
Refractive index	1.47
Light transmission above 350 nm	>95%
Density	2.23 g cm <sup>-3</sup>
Pressure of qualification test	700 bar (70 MPa)
Diameter shrinking at 250 bar	1.25 mm (0.3%)
Absolute internal air pressure	0.7 bar (70 kPa)
Hole diameters (penetrator and vacuum port)	20 mm, 5 mm

Table 1: Data on the OM glass sphere.

<sup>13</sup>Nautilus Marine Service GmbH, <http://www.nautilus-gmbh.de>

442

443 hemisphere” is painted black on its internal surface and the other, “front  
444 hemisphere” is transparent. The front hemisphere houses the PMT and the  
445 magnetic shielding held in place by the optical gel. The back hemisphere  
446 has two drilled holes to accommodate the electrical connection via a pene-  
447 trator and a vacuum port. Around both holes a flat surface is machined on  
448 the outside of the sphere for the contact of the single O-ring ensuring water  
449 tightness. The back hemisphere is also equipped with a manometer readable  
450 from the outside. The two glass halves have precisely machined flat equato-  
451 rial surfaces in direct contact (glass/glass) without any gasket or interface.  
452 The risk of implosion and the consequences on the structure were consid-  
453 ered since its potential energy is of the order of a megajoule (200 g of TNT)  
454 at the depth of the detector. Based on tests performed by DUMAND [12]  
455 and further tests performed off Corsica in the year 2000 by the ANTARES  
456 Collaboration, it has been concluded that the implosion of a glass sphere at  
457 the ANTARES depth would provoke the loss of the two other spheres of the  
458 same storey (at centre distances of 770 mm) but not of spheres on adjacent  
459 storeys (at a distance of 14.5 m), and would not cut or damage the cable.  
460 The rigid storey mechanical frame would be distorted but not destroyed by  
461 the implosion.

### 462 3.1.2.3. *Optical gel.*

463 The optical coupling between the glass sphere and the PMT is achieved  
464 with optical gel. The chosen gel is a two-component silicon rubber provided  
465 by the Wacker company<sup>14</sup>. The mixture of the components is made in the  
466 ratio 100:60. After curing and polymerization, lasting 4 hours at ambient  
467 temperature, the optical gel reaches an elastic consistency soft enough to  
468 absorb the sphere diameter reduction by the deep sea pressure (1.2 mm)  
469 and stiff enough to hold the PMT in position in the sphere. The optical  
470 properties of the gel have been measured in the laboratory: the absorption  
471 length is 60 cm and the refractive index is 1.404 for wavelengths in the blue  
472 domain.

### 473 3.1.2.4. *Magnetic shield.*

474 At the ANTARES site, the Earth’s magnetic field has a magnitude of  
475 approximately 46  $\mu\text{T}$  and points downward at 31.5° from the vertical. Un-

---

<sup>14</sup>Silgel 612 A/B; Wacker-Chemie AG, <http://www.wacker.com>

476 corrected, the effect of this field would be a significant degradation of the  
477 TTS, of the collection efficiency and of the charge amplification of the PMT.  
478 A magnetic shield is implemented by surrounding the bulb of the PMT with  
479 a hemispherical grid made of wires of  $\mu$ -metal<sup>15</sup> closed by a flat grid on the  
480 rear of the bulb. This provides a magnetic shielding for the collection space  
481 and for the first stages of the amplification cascade. The efficiency of the  
482 screening becomes larger as the size of the mesh is reduced and/or the wire  
483 diameter is increased, however the drawback is a shadowing effect on the  
484 photocathode. The compromise adopted by the ANTARES Collaboration, a  
485 mesh of  $68 \times 68 \text{ mm}^2$  and wire diameter of 1.08 mm, results in a shadowing  
486 of less than 4 % of the photocathode area while reducing the magnetic field  
487 by a factor of three. Measurements performed in the laboratory show that  
488 this shielding provides a reduction of 0.5 ns on the TTS and a 7 % increase  
489 on the collected charge with respect to a naked, uniformly illuminated PMT.

#### 490 *3.1.2.5. HV power supply.*

491 To limit the power consumption of the HV power supply a high voltage  
492 generator based on the Cockroft-Walton [13] scheme is adopted. The HV  
493 generator chosen for the ANTARES detector is derived from the model de-  
494 veloped for the AMANDA experiment<sup>16</sup>, and is manufactured by the iseg  
495 company<sup>17</sup>. It has two independent high-voltage chains. The first chain  
496 produces a constant focusing voltage (800 V) to be applied between photo-  
497 cathode and first dynode. The second chain gives the amplification voltage,  
498 which can be adjusted from 400 V to 1600 V by an external DC voltage.  
499 The HV generator is powered by a 48 V DC power supply and has a typical  
500 consumption of 300 mW.

501 The signals of the anode, of the last dynode and of the last-but-two dyn-  
502 ode of the PMT are routed to the electronics container together with the  
503 PMT ground. A low level voltage image of the actual HV is provided for  
504 monitoring purpose.

#### 505 *3.1.2.6. Internal LED.*

506 On the rear part of the bulb of the PMT, a blue LED is glued in such  
507 a way to illuminate the pole of the photocathode through the aluminium

---

<sup>15</sup>Sprint Metal, Ugitech, <http://www.ugitech.com>

<sup>16</sup><http://icecube.wisc.edu/>

<sup>17</sup>PHQ7081-20; iseg Spezialelektronik GmbH, <http://www.iseg-hv.de>

508 coating, which acts as a filter of large optical density (optical density  $\approx 5$ ).  
509 This LED is excited by an externally driven pulser circuit and is used to  
510 monitor the internal timing of the OM.

### 511 *3.1.2.7. Link with the electronics container.*

512 The electrical connection of the OM to the electronics container is made  
513 with a penetrator<sup>18</sup> (Ti socket with polyurethane over moulding). The as-  
514 sociated cable contains shielded twisted pairs for the transmission of power,  
515 the control of the LED pulser and the setting and monitoring of the DC  
516 command voltage of the PMT base. One pair is used to transmit the an-  
517 ode and the last dynode signals. This pseudo differential transmission pair  
518 has the advantage of reducing the noise and enhancing the output signal by  
519 approximately a factor of two when the subtraction is done at the readout  
520 electronics. The last pair is used to transmit signals from the last-but-two  
521 dynode, together with the ground, for the treatment of very high amplitude  
522 signals.

### 523 *3.1.2.8. Final assembly and tests.*

524 The assembly starts with the pouring of the gel into the front hemisphere  
525 and a precise sequence of out-gasing is applied in order to avoid the appear-  
526 ance of bubbles during the polymerization phase. Then, the cage and the  
527 PMT are positioned by tools which ensure a defined position with respect  
528 to marks on the hemisphere. These marks are also used to mount the OM  
529 on its support structure, giving each PMT a well-defined and reproducible  
530 orientation with respect to the storey mechanical structure.

531 After the gluing of the LED, the cabling of the base to the pig-tail of the  
532 penetrator and the connection of the PMT, the back hemisphere is placed  
533 in contact with the front one. Closure is obtained by establishing an un-  
534 derpressure of  $\approx 300$  mbar inside the sphere. The equatorial seam is sealed  
535 externally with butyl rubber sealant which is protected by a sealant tape.  
536 Figure 7 shows an assembled OM. The same test bench as for the naked  
537 PMT is used to test the OM. Dark count rate, gain and LED functionality  
538 are checked.

---

<sup>18</sup>EurOcéanique S.A., part of MacArtney Underwater Technology,  
<http://www.macartney.com>





Figure 7: Photograph of an optical module. It is positioned on a mirror to better show the full assembly.

539 *3.1.3. OM support*

540 The OM support is made of a stamped Ti grade 2 conical plate (OD = 280 mm)  
541 on which the OM is pulled by a pair of Ti wires ( $\varnothing = 4$  mm) under tension  
542 running around the glass sphere (Figure 8). The wires are designed to follow  
543 a great circle of the sphere, which results in their stable equilibrium position  
544 on the glass surface. A set of 5 rubber pads are inserted between the metal  
545 parts and the OM to protect the glass surface and to keep the assembly under  
546 tension in spite of the pressure shrinking. Tests at 250 bar (25 MPa) showed  
547 that the support allows the OM to sustain a test torque of 5 Nm without  
548 rotating. The titanium plate is also the interface to the optical module frame.

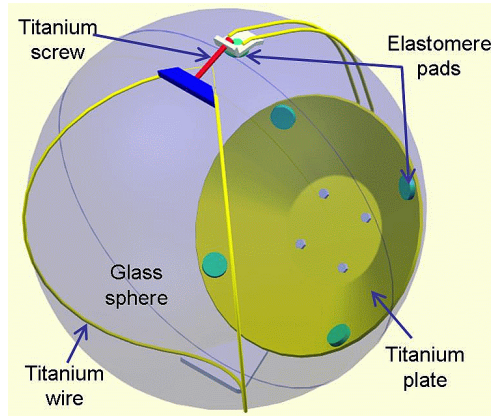


Figure 8: OM support mechanics.

549 *3.2. Storey*

550 *3.2.1. Optical module frame*

551 The role of the optical module frame (OMF) is to hold the three OMs  
 552 of the storey, the associated LCM container and to connect both mechanical  
 553 terminations of the EMCs. The OMF and its connections are specified up  
 554 to a breaking load of 7 tons. Some OMFs also hold optional equipment such  
 555 as LED beacons [14], positioning hydrophones and certain oceanographic  
 556 sensors.

557 The OMF (Figure 9) is a welded vertical structure of Ti (grade 2; chosen  
 558 for the ease of welding) and of three-fold periodic symmetry around the  
 559 vertical axis. The main elements are:

- 560 ● at the top and bottom, two rings (ID = 85 mm) on which are locked  
 561 the EMC mechanical terminations;
- 562 ● three shaped tubes (OD = 33.4 mm, thickness = 3.38 mm) connecting  
 563 these rings vertically with an overall height of 2.12 m (2 m between  
 564 EMC mechanical terminations);
- 565 ● four spacers of triangular shape made of 12 mm diameter rod between  
 566 the three tubes:
  - 567 – the bottom triangle holds the LCM container on the vertical axis  
 568 of the OMF;
  - 569 – the next spacer stiffens the structure at the height of the 3 OM  
 570 fixture plates (80×80×5 mm), welded on each tube at a distance  
 571 of 195 mm from the axis;

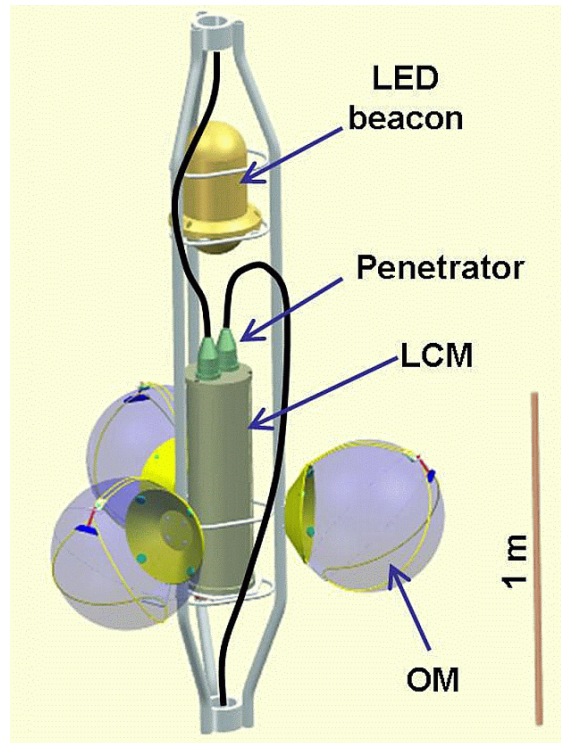


Figure 9: OMF equipped with the 3 OMs, the LCM and an LED beacon. The mechanical parts used for fixing cables toward the upper and the lower storeys are omitted.

572           – the two top spacers are used to hold the optional LED beacon.

573       All OMFs were validated by applying a traction load of 80 kN, which is  
574       in fact higher than the load resulting from the design rule of 7 tons.

### 575   3.2.2. Local control module

#### 576   3.2.2.1. Container.

577       The housing of the readout electronics is a Ti grade 5 container made  
578       of a hollow cylinder (600 mm long, 179 mm outer diameter and 22 mm  
579       wall thickness) closed by two end caps (30 mm thick). The top end cap  
580       accommodates the two large penetrators of the EMC linking the storey to  
581       its upper and lower adjacent storey. The bottom end cap accommodates  
582       three connectors linking the LCM to its three optical modules. In some of  
583       the LCMs, a 4<sup>th</sup> connector is needed for additional equipment. The fixation  
584       of the end caps on the cylinder and of the whole container on the OMF is

585 made with three external threaded rods of 6 mm diameter in Ti grade 2.  
586 The thickness of the cylinder and of the end-caps was optimised by Finite  
587 Element Method analysis with the goal to stay within the yield strength  
588 of the material at an external pressure of 310 bars. The calculations were  
589 tested by the collapse under pressure of an Al alloy container of the same  
590 configuration. Ti grade 5 was chosen for its yield strength around 900 MPa,  
591 compared to that of grade 2 which is around 300 MPa.

### 592 3.2.2.2. *Electronics.*

593 In order to optimally fill the cylindrical volume offered by the container,  
594 a dedicated crate was developed. This crate accepts circular shaped printed  
595 circuit boards plugged on a backplane which distributes the signals as well  
596 as the DC power supplied by the local power box. The crate was designed  
597 to ensure that its mechanical structure acts as a medium that transfers the  
598 heat produced by the electronics to the Ti cylinder in contact with the water.  
599 After evaluating different metals, the final choice was made for aluminium  
600 which can guarantee good performance with light weight and at an affordable  
601 price. Furthermore, boards having high power consumption are equipped  
602 with metal cooling bases which are in thermal contact with the crate.

603 Most of the LCMs contain the same set of electronics cards. However, due  
604 to the segmentation of a line in sectors, one in five LCMs, called Master LCM  
605 or MLCM, acts as a master for other LCMs of the same sector and houses  
606 additional boards. Other differences between individual LCMs are due to  
607 electronics necessary for optional equipment on the storey (hydrophone, LED  
608 beacon, ...).

609 A standard LCM contains the following elements:

- 610 • LPB. Fixed on the crate, the local power box is fed by the 400 V DC  
611 from the bottom of the line, and provides the 48 V for the optical  
612 modules and several different low voltages for the electronics boards.  
613 An embedded micro-controller allows the monitoring of the voltages,  
614 the temperatures and the current consumptions as well as the remote  
615 setting of the 48 V for the OMs.
- 616 • CLOCK. The clock reference signal coming from shore reaches the bot-  
617 tom of the line where it is repeated and sent to each sector. Within  
618 a sector, the clock signal is daisy-chained between LCMs. The role of  
619 the CLOCK card is to receive the clock signal from the lower LCM,  
620 to distribute it on the backplane and to repeat it toward the upper

621 LCM of the sector. It also has the capability to pass commands on the  
622 backplane which are coded within the clock signal.

- 623 • ARS\_MB (Figure 10). The ARS motherboards host the front-end elec-  
624 tronics of the OMs (one board per OM). This front-end electronics con-  
sists of a custom-built Analogue Ring Sampler (ARS) chip [9] which



Figure 10: The ARS\_MB board with the 2 ARSs (labelled 16 and 15). The 3<sup>rd</sup> one (top right, labelled 12) is foreseen for trigger purposes.

625 digitizes the charge and the time of the analogue signal coming from  
626 the PMTs, provided its amplitude is larger than a given threshold.  
627 The level of this threshold is tuneable by slow-control commands. The  
628 analogue signal is integrated by an AVC (Amplitude to Voltage Con-  
629 verter) to obtain the charge which is digitized by an ADC. The ARS  
630 can also operate like a flash-ADC using analog memories with a sam-  
631 pling tuneable down to sub-nanosecond values. The output consists of  
632 a waveform of 128 amplitude samples. The arrival time is determined  
633 from the signal of the clock system in the LCM and from a TVC (Time  
634 to Voltage Converter) which provides a sub-nanosecond resolution. To  
635 minimise the dead time induced by the digitization, each ARS\_MB card  
636 is equipped with 2 ARSs working in a token ring scheme. For a storey  
637 with an optical beacon, a 4<sup>th</sup> ARS\_MB is installed to digitize the signals  
638 sent by the internal PMT of the beacon.  
639

- 640 • DAQ/SC (Figure 11). The DAQ/Slow-Control card host the local pro-  
 641 cessor and memory. The processor is a Motorola MPC860P which  
 642 runs the VxWorks real time operating system<sup>19</sup> and hosts the software  
 643 processes [8]. These processes are used to handle the data from the  
 644 ARS chips and from the slow control, respectively. The processor has  
 645 a fast Ethernet controller (100 Mb s<sup>-1</sup>) that is optically connected to  
 an Ethernet switch in the MLCM of the corresponding sector. Three

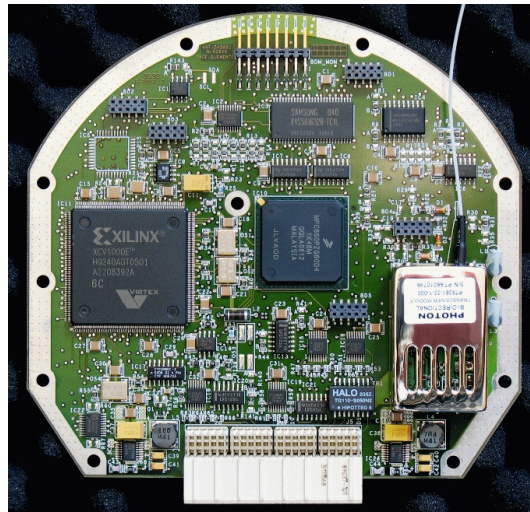


Figure 11: The DAQ/SC board holding the processor (centre), the FPGA (left) and the optical link to the MLCM (right).

- 646 serial ports, two with RS485 links and one with RS232 links, using the  
 647 MODBUS protocol<sup>20</sup> are used to handle the slow control signals. The  
 648 specific hardware for the readout of the ARS chips and data format-  
 649 ing is implemented in a high density field programmable gate array<sup>21</sup>.  
 650 The data are temporarily stored in a high capacity memory (64 MB  
 651 SDRAM) allowing a de-randomisation of the data flow.  
 652

  - 653 • COMPASS\_MB (Figure 12). The compass motherboard hosts a TCM<sup>22</sup>  
 654 sensor which provides heading, pitch and roll of the LCM (i.e. of the

<sup>19</sup>Wind River, <http://www.windriver.com>

<sup>20</sup><http://www.modbus.org>

<sup>21</sup>Virtex-EXCV1000E, <http://www.xilinx.com>

<sup>22</sup>PNI Sensor Corp., <http://www.pnicorp.com>

655 OMF) used for the reconstruction of the line shape and PMT positions.  
656 The heading is measured with an accuracy of  $1^\circ$  over the full cycle and  
657 the tilts with an accuracy of  $0.2^\circ$  over a range of  $\pm 20^\circ$ . The same  
658 card supports two micro-controllers dedicated to the slow control: they  
659 control the measurements of various temperatures and the humidity,  
and set and monitor the PMT high voltages.

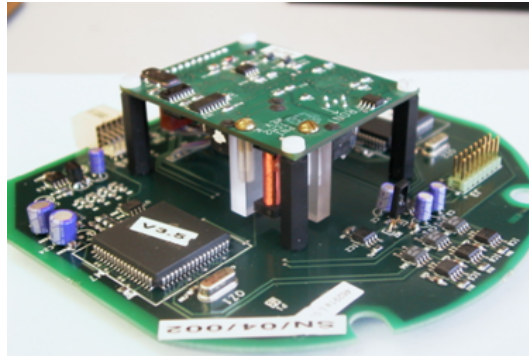


Figure 12: The COMPASS\_MB equipped with a TCM2 sensor on a raised daughter card.

660

661 For LCMs performing acoustic functions (cf. Section 3.8), there are three  
662 additional cards: one housing a pre-amplifier, one a CPU and the third a  
663 digital signal processor. These cards are commercial products from ECA<sup>23</sup>,  
664 re-shaped to fit in the crate.

665 An MLCM holds the following additional cards:

- 666 • BIDICON. It communicates via bi-directional optical fibres with the  
667 four other LCMs of the sector, and performs the electrical $\leftrightarrow$ optical con-  
668 version of signals transmitted via the backplane to or from the SWITCH  
669 card.
- 670 • SWITCH. An Ethernet switch which consists of a combination of eight  
671  $100 \text{ Mb s}^{-1}$  ports and two  $1 \text{ Gb s}^{-1}$  ports<sup>24</sup>. One of the  $100 \text{ Mb s}^{-1}$  ports  
672 is connected to the processor of the MLCM and four to the BIDICON  
673 card via the backplane. One of the two  $\text{Gb s}^{-1}$  ports is connected to a  
674 Dense Wavelength (De)-Multiplexer (DWDM) transceiver.

---

<sup>23</sup>ECA S.A., <http://www.eca.fr>

<sup>24</sup>Allayer AL121 and AL1022 respectively.

- 675 • DWDM (Figure 13). The role of the transceiver is to perform the  
 676 electrical↔optical conversion for the full sector and to communicate  
 677 with the shore via the SCM located at the bottom of the line. It  
 678 is electrically connected to the SWITCH card via coaxial cables and  
 679 optically to the SCM via two uni-directional optical fibres (Rx and Tx)  
 680 at a connection speed of  $1 \text{ Gb s}^{-1}$ . For each MLCM (i.e. sector) of a  
 681 line, the laser mounted on the card has a specific frequency chosen in  
 682 the range from 192.1 to 194.9 THz, the frequency spacing being 400  
 GHz.

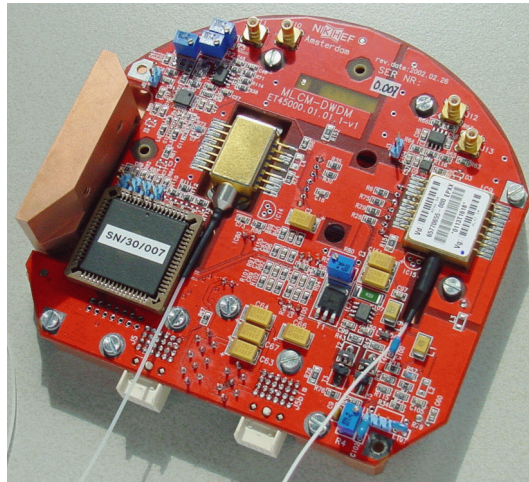


Figure 13: The DWDM board.

683

684 Figure 14 shows an MLCM crate equipped with the full set of the elec-  
 685 tronics cards. A description of the components in the SPM/SCM container  
 686 will be given later in the BSS Section 3.4.3.

### 687 3.3. *Electro-optical mechanical cable (EMC)*

688 The EMC cable has three roles:

- 689 • optical data link: 21 single mode optical fibres ( $\varnothing=9/125/250 \mu\text{m}$ ) run  
 690 along the cable;
- 691 • power distribution: 9 electrical conductors (Cu section =  $1 \text{ mm}^2$  with  
 692 insulation  $\varnothing = 2.5 \text{ mm}$ );
- 693 • mechanical link: breaking tension above 177 kN.



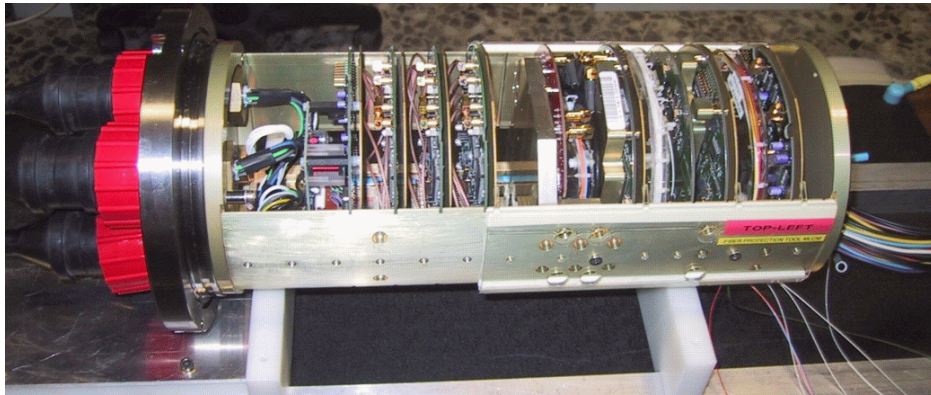


Figure 14: The crate of an MLCM equipped with the electronics boards.

694 To facilitate the line handling and deployment with its cumulative length  
 695 of  $\approx 480$  m, the minimal allowed radius of curvature of the cable was specified  
 696 to be less than 300 mm (180 mm for the naked core).

697 The cable, developed under the responsibility of EurOcéanique<sup>18</sup> is assembled  
 in successive layers as shown in Figure 15. The two internal layers are

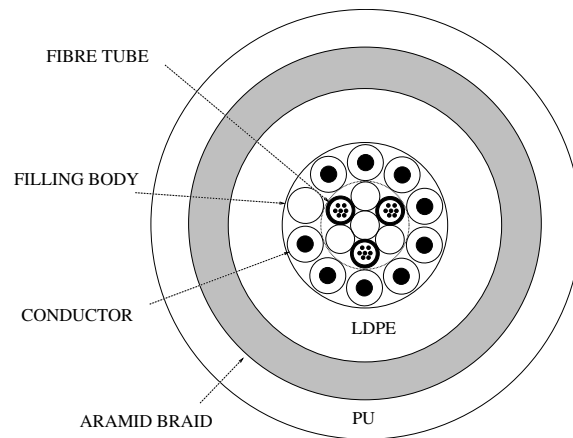


Figure 15: Cross section of the EMC. From centre to outside one can distinguish the layer with 3 tubes, each housing 7 optical fibres, the layer with 9 copper conductors, the LDPE jacket, the aramid braid and the polyurethane sheath. The external diameter is 30 mm.

698 assembled with silicon compound filling the space between the elements. Wa-  
 699 ter can penetrate through the 2 external layers, while the inner polyethylene  
 700 jacket acts as a water barrier. The polyurethane (PU) sheath is in contact  
 701

702 with the water. Its role is to protect the aramid braid and the cable be-  
 703 fore and during deployment. The two outer layers end inside the mechanical  
 704 termination where the aramid braid is firmly held by a cone locking-system  
 705 and the rest of the cable, called the “core”, continues for a few meters  
 706 to the LCM penetrators. Each section sustained a static test tension of 50 kN.  
 707 During this test, the insulation of electrical conductors and the attenuation  
 708 on the optical fibres are controlled. The cable length between the mechanical  
 709 terminations is 98 m for the bottom cable section and 12.5 m for the 25 other  
 710 sections of a line (including the passive section linking the top storey to the  
 711 buoy), resulting in a pitch between optical modules of 14.5 m. The actual  
 712 length of each section delivered was measured under a tension of one ton,  
 713 with an accuracy of  $\pm 5$  mm, and the results were recorded in a database as  
 714 input to the line shape reconstruction. Figure 16 gives a schematic view of  
 715 the top and bottom mechanical terminations and their PU bending limitors.

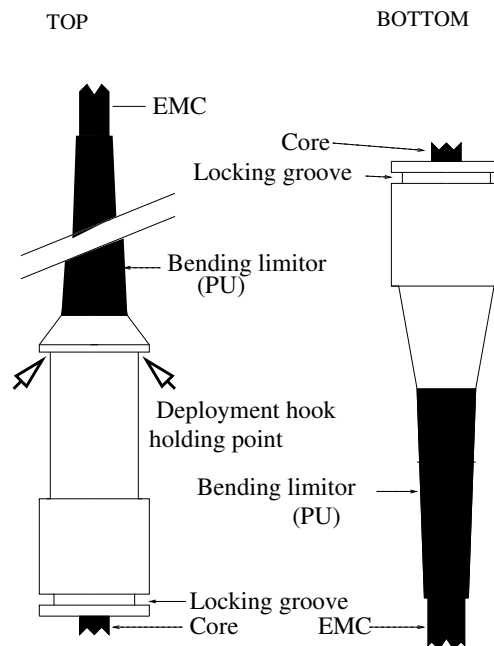


Figure 16: Mechanical termination of an EMC.

716

717 Two different types of LCM penetrators are mounted at the ends of the  
 718 core: a pair of water-blocking (WB) penetrators for the sections located  
 719 between sectors and a less expensive pair of non-water-blocking (NWB) pen-

etrators elsewhere. In case of a flooded cable, the WB type stops the propagation of the water along the cable and thus limits the flooded part of the line to one sector (the WB penetrator only stops water propagation from the cable to the container and not in the opposite direction). Figure 17 gives a schematic view of the NWB penetrator (left) and of the WB penetrator (right). In both cases, the fibre tubes are mechanically blocked in an epoxy moulding, itself blocked in the penetrator body to avoid extrusion when the cable is subject to water pressure.

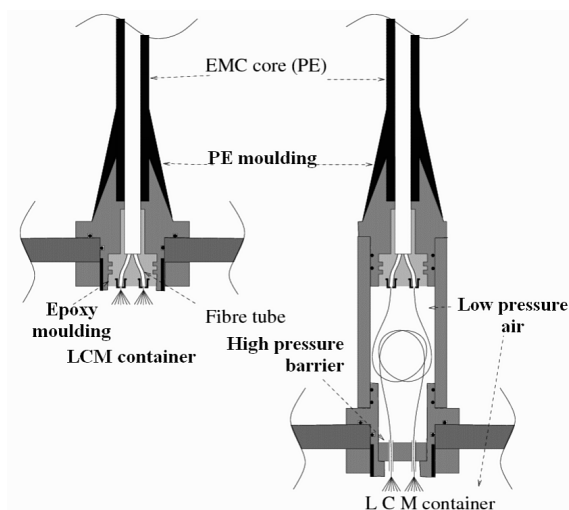


Figure 17: EMC penetrators of the LCM container. Left: non water blocking. Right: water blocking. For clarity, the 3rd fibre tube and the 9 conductors are not shown.

727

728 When subjected to a uniform horizontal sea current, as present at the  
 729 ANTARES site, the 3-fold periodic symmetry of the storey induces a torque  
 730 which is a function of the actual azimuth of the storey. The storey is in stable  
 731 equilibrium when one of the three OMs is upstream of the current. From  
 732 measurements performed in a pool, the torque was found to be proportional  
 733 to the square of the current with a proportionality constant of  $9.47 \text{ N s}^2 \text{ m}^{-1}$ .

734

735 Between two adjacent storeys, the EMC acts as a torsion spring tending to  
 736 keep them at the same relative angle. This torque was measured as a function  
 737 of the cable tension on a prototype and found to be proportional to the  
 738 cable torsion angle per unit length and to the tension with a proportionality  
 739 constant of  $1.3 \times 10^{-3} \text{ m}^2 \text{ rad}^{-1}$ . In order to specify the minimum torsion  
 740 strength of the cable, the torsion behaviour of the line was simulated using  
 the above data and for very unfavorable environmental conditions: uniform

741 sea current at  $30 \text{ cm s}^{-1}$  slowly increasing in the azimuth angle for several  
742 turns. The resulting specification was a maximum torsion angle change per  
743 unit length of  $\pm 45^\circ \text{ m}^{-1}$ .

#### 744 3.4. Bottom string structure

745 The function of the BSS (Figure 18) is to anchor the line to the seabed  
746 with the capability of a recovery. The BSS is made of two parts: an unre-  
747 coverable dead weight laid on the seabed and a recoverable part sitting on  
748 top. The two parts are connected by a release system remotely controlled by  
acoustic signals.

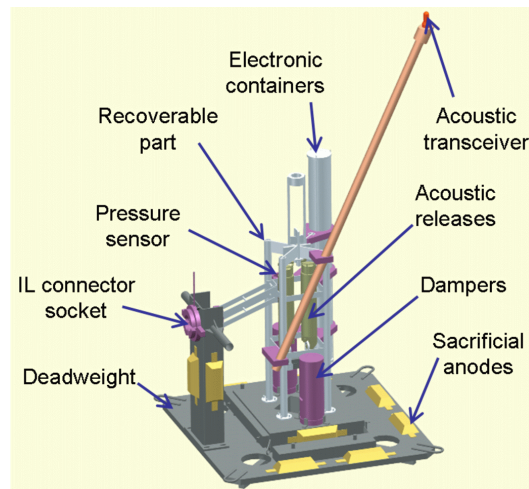


Figure 18: The ANTARES Bottom String Structure.

749

##### 750 3.4.1. Dead weight

751 The dead weight is a horizontal square plate made of 50 mm thick carbon  
752 steel. The line stability requires a dead weight of 1270 kg in water, which  
753 means 1.5 tons of steel. Therefore, the dimension of the square side is 1.8 m,  
754 resulting in a ground pressure of 4 kPa, while the seabed is believed to  
755 sustain safely a pressure up to 5 kPa. Four steel “wings” are welded below  
756 the square plate to improve the anchoring in the seabed sediment. The total  
757 wet surface of steel is  $9.5 \text{ m}^2$ . To avoid the galvanic corrosion of this large  
758 surface in contact with the sea water, 9 plates of Al-Zn-In alloy, the so-called

759 sacrificial anodes<sup>25</sup>, are welded on the steel surface with a total mass of 68 kg.

760 The line is linked to the junction box by the interlink cable (IL), an  
761 electro-optical cable laying on the seabed and connected to the line at the  
762 level of the BSS by an underwater mateable connector:, developed by ODI  
763 company<sup>26</sup>.

764 The remote line release implies an automatic disconnection system for  
765 the IL cable: the plug of the IL is fixed to the dead weight while the socket  
766 is located on the recoverable part of the BSS, at the end of a pivoting arm in  
767 such a way that it is extracted from the plug at the beginning of the ascent.  
768 In order to slow down the speed of extraction ( $\leq 5 \text{ cm s}^{-1}$  as recommended  
769 by the manufacturer) and to guide the disconnection phase of the ascent,  
770 two vertical damping systems are mounted between the two parts of the  
771 BSS: a pair of pistons on the dead weight matching a pair of cylinders on the  
772 recoverable part. These parts are in LDPE and/or PETP, the piston has a  
773 diameter of 150 mm and a used height of 670 mm. The damping effect was  
774 adjusted in pool tests. Finally, the piston/cylinder gap was set to 0.8 mm  
775 and a set of grooves was machined along the pistons to avoid suction effect  
776 in water and water inlets were drilled through the cylinder.

#### 777 *3.4.2. Release system*

778 The BSS holds two lithium battery powered transponders<sup>27</sup> in Ti cylinders  
779 which are equipped with release mechanism. The releases are mounted on the  
780 recoverable part of the BSS in a redundant system which includes a chain,  
781 made of Ti and steel, engaged inside a steel part belonging to the dead weight.  
782 The chain is pre-tensioned to avoid a gap between the two components of  
783 the BSS. The acoustic beacon capability of the transponders is employed  
784 in the Low Frequency Long Baseline (LFLBL) positioning and navigation  
785 system to monitor the position of the line anchor during its deployment and  
786 to determine its geodetic location with a precision of  $\approx 1 \text{ m}$ .

#### 787 *3.4.3. Recoverable part*

788 In addition to the already mentioned transponders, the recoverable part  
789 of the BSS holds various equipment:

---

<sup>25</sup>BAC Corrosion Control A/S, <http://www.bacbera.dk>

<sup>26</sup>Ocean Design Inc. (ODI), <http://www.odi.com>

<sup>27</sup>Type RT 861 B2T; IXSEA/Oceano, <http://www.ixsea.com>

- 790 • a 1.8 m long Ti container housing the power module and the control  
791 electronics (SPM/SCM) of the line;
- 792 • a high resolution pressure meter, used for line positioning;
- 793 • an acoustic transceiver at the top of a 3.6 m long rod of glass-epoxy,  
794 used as a reference emitter for the High Frequency Long Base Line  
795 (HFLBL) positioning system;
- 796 • optional sound velocimeter, laser beacon, seismometer depending on  
797 the line [15];
- 798 • a weight to keep the line vertical and under enough tension after release,  
799 even when the buoy reaches the sea surface.

800 The recoverable part of the BSS is a welded Ti (grade 2) structure sitting  
801 on top of a square steel weight (950 mm side length and 160 mm thickness)  
802 of 1140 kg total mass (9.6 kN weight in water) and with 2.5 m<sup>2</sup> wet surface  
803 of steel. Depending on the actual equipment of the line, this mass is ad-  
804 justable by a set of steel plates welded on the weight. The steel parts are  
805 anode protected in the same way as the dead weight, with three anodes with  
806 a total mass of 30 kg. After two years of immersion of prototypes, the anode  
807 consumption rate was measured to be  $\approx 300$  g per year and per square meter  
808 of wet steel. This value can be extrapolated to an approximate lifetime of  
809 the anodes of 40 years.

810 The SPM/SCM electronics container is the assembly of two cylinders sim-  
811 ilar to those of the LCMs and is fixed vertically on the structure (Figure 18).  
812 The SPM part, at the top, contains transformers/rectifiers which deliver the  
813 five 400 V DC supplies needed for the sectors, starting from the 480 V AC  
814 provided by the junction box. An embedded micro-controller operates the re-  
815 mote powering of sectors. Voltages, temperatures and current consumptions  
816 are monitored. The micro-controller can also detect anomalies and is pro-  
817 grammed to turn off the power in case of over-consumption. Like a standard  
818 LCM container, the SCM cylinder houses a crate equipped with COMPASS,  
819 CLOCK and DAQ cards. In order to perform the distribution of the clock  
820 signal to the sectors, the SCM crate houses specific boards called:

- 821 • SCM.WDM (Wavelength Division Multiplexing) (Figure 19) which re-  
822 ceives the 20 MHz clock signal via an optical link from the shore and  
823 converts it to an electrical signal which is distributed on the backplane.  
824 For redundancy, the clock is transmitted on two fibres from the shore

825

and in case of failure of one fibre, the WDM card automatically switches to the other.

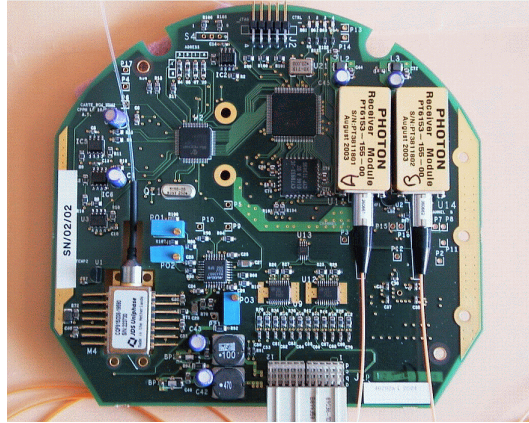


Figure 19: The SCM\_WDM board.

826

- 827 • REP: its role is to operate the reverse conversion. It is equipped with  
828 three fibre outputs and two such cards are needed to distribute the  
829 clock signals to the five sectors.

830 To communicate with the shore, the SCM is equipped with a DWDM  
831 board similar to the MLCM one but working at  $100 \text{ Mb s}^{-1}$  and using its own  
832 DWDM channel. The pair of fibres of this DWDM is connected, as well as  
833 the 5 pairs of fibres coming from the sectors to 6 channels of a 1-to-8 passive  
834 optical mux/demux<sup>28</sup> performing the merging/separation of the 6 colours.  
835 The BSS being equipped with an acoustic transceiver, the appropriate cards  
836 are present in the SCM crate.

### 837 3.5. Top buoy

838 The top buoy<sup>29</sup> is made of syntactic foam qualified for a depth of 3000 m  
839 and with a density around  $0.5 \text{ g cm}^{-3}$ . The foam is moulded into an oval  
840 shape (horizontal diameter = 1347 mm, height = 1530 mm) with a hole along  
841 the vertical axis where a Ti rod is inserted. The buoy is held on the rod by

---

<sup>28</sup>Multi-Channel Mux/Demux Module 400 GHz spacing; JDS Uniphase Corp., <http://www.jdsu.com>

<sup>29</sup>TRELLEBORG CRP, <http://www.trelleborg.com/en/offshore>

842 a pair of Ti disks. The last EMC section is fixed on the bottom end of this  
843 rod and, for the deployment, a releasable transponder is fixed to the top end.  
844 The mass of the equipped buoy is 782 kg and its buoyant force 6.7 kN.

### 845 *3.6. Mechanical behaviour of a line*

846 Three rules govern the stability of a line.

- 847 1. The line must remain firmly anchored on the seabed and must be held  
848 close to vertical even in the presence of the strongest sea current con-  
849 sidered ( $30 \text{ cm s}^{-1}$ ). In all situations, the horizontal displacement of  
850 any part of the line must be smaller than the horizontal line spacing (60  
851 m) to avoid any possible contact between two lines. The fact that, in a  
852 uniform sea current, two adjacent lines will lean in the same direction  
853 gives an extra safety factor.
- 854 2. The tension in the release chain while the line is on the seabed, must  
855 be above 4 kN in order to overcome any possible blocking of the release  
856 systems and in order to reach the surface in one hour or less.
- 857 3. During the recovery, while the buoy is floating on the surface, the EMC  
858 tension must be above 2 kN everywhere along the line to allow a safe  
859 operation of an automatic hook system which must slide down along  
860 the EMC.

861 The buoyancy is provided by the top buoy but also by the storeys, since  
862 each OM has a buoyant force of 0.22 kN. A sector of five storeys with their  
863 cables has a buoyant force of 1.42 kN. The weight is mainly provided by  
864 the BSS recoverable part and, until the release, its dead weight. The global  
865 recovery force is the small difference between two large quantities: the weight  
866 in air of the line (without the dead weight) which amounts to 5.5 tons and the  
867 weight of the sea water displaced by the line (6 tons). To limit the uncertainty  
868 on this force to 10%, a measurement of the mass and of the volume of all the  
869 line components within 0.5% is required. Table 2 summarises the resulting  
870 tension along the line for three static periods of the life of a line without sea  
871 current:

- 872 • during the deployment, held by the deep sea cable of the surface boat  
873 (maximum stress conditions);
- 874 • in operation on the seabed (rule 2 above applies);
- 875 • during the recovery, while the buoy floats at the surface (rule 3 applies).



876 These data are based on a detailed list of measurements and calculations  
 877 which take the acceleration of gravity of  $9.805 \text{ m s}^{-2}$  (computed for the site  
 878 location), the specific mass of  $1033 \text{ kg m}^{-3}$  for deep sea water,  $998 \text{ kg m}^{-3}$   
 879 for fresh water (in which some components were weighed) and 0.9% for the  
 880 volume shrinking of the three OMs.

	Deployment	Seabed	Sea surface
Deployment cable	7.7		
26 <sup>th</sup> EMC section	14.3	6.6	2.0
21 <sup>th</sup> EMC section	15.7	8.0	3.4
16 <sup>th</sup> EMC section	17.3	9.5	4.8
11 <sup>th</sup> EMC section	18.6	10.8	6.3
6 <sup>th</sup> EMC section	20.0	12.4	7.6
1 <sup>st</sup> EMC section	21.4	13.6	8.9
Release chain	12.5	4.7	

Table 2: Tension (kN) at the bottom of the specified cable or chain, for 3 periods in the life of the line and at 8 positions along the line.

881 Figure 20 shows the results of a calculation based on the buoyant and  
 882 drag forces on horizontal displacements for a current of  $25 \text{ cm s}^{-1}$ . Even in  
 883 this unfavorable condition, the maximum displacement of the line compared  
 884 to the vertical is  $\lesssim 25 \text{ m}$ . The displacement scales with the square of the  
 885 current velocity. Such a current increases the cable tension by 0.6% in the  
 886 worst case, at the bottom of the line, scaling with the fourth power of the  
 887 velocity.

### 888 3.7. Timing calibration devices

889 For the timing calibration of the apparatus, pulsed light sources are used.  
 890 They are of two types: LED beacons and laser beacons [14]. They are  
 891 distributed in specific locations throughout the detector.

#### 892 3.7.1. LED beacons

893 An LED beacon is a point-like light source which can be triggered re-  
 894 motely. The electronics and individual light sources (LEDs) are enclosed in  
 895 a glass container (same manufacturer as the OM sphere). This container is a  
 896 cylinder completed by two hemispheres and joined by titanium flanges. The  
 897 overall dimensions are 210 mm for the outer diameter and 443 mm for the full  
 898 length. They are positioned at the top of the OMF (Figure 9) on storeys 2, 9,

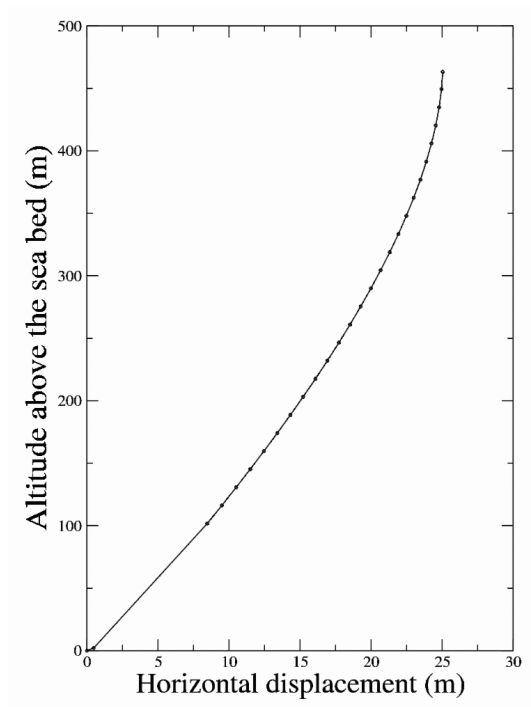


Figure 20: Line shape for a sea current velocity of  $25 \text{ cm s}^{-1}$  velocity. The horizontal scale is enhanced to better illustrate the line shape.

899 15 and 21 (numbering from the bottom storey) of each line. The pulsed light  
 900 source is composed of 36 blue<sup>30</sup> LEDs in groups of six on 6 printed circuit  
 901 boards (Figure 21). These boards are assembled into a hexagon configuration  
 902 and contain the pulser circuits and components to allow an individual tuning  
 903 of the timing for each LED. The geometrical arrangement of the LEDs is such  
 904 that the emitted light is almost isotropic in azimuth. The number of boards  
 905 as well as the number of LEDs flashing can be varied. A pencil PMT<sup>31</sup> sits  
 906 in the centre of the hexagon and is exposed to the emitted light in order to  
 907 provide the precise pulse time.

<sup>30</sup>HLMP-CB15; Agilent Technologies Inc., <http://www.agilent.com>

<sup>31</sup>H6780-03; Hamamatsu, <http://www.hamamatsu.com>

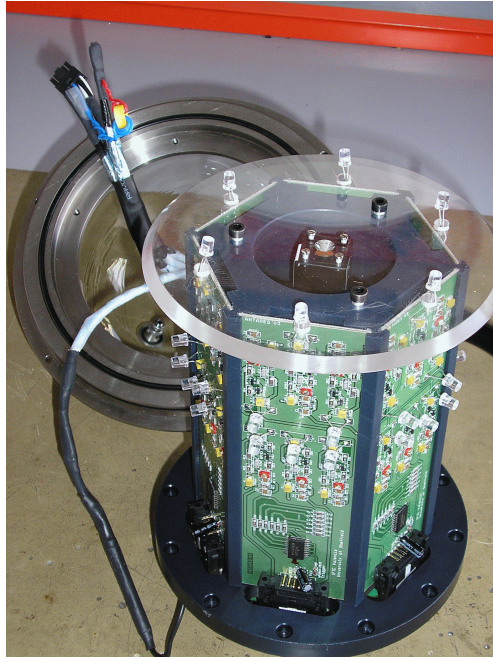


Figure 21: The electronic boards and light sources of an LED beacon.

908 *3.7.2. Laser beacons*

909 Due to their positions, LED beacons are not efficient for the timing cal-  
910 ibration of the lowest storeys of the lines and between lines. Hence, they  
911 are complemented by light sources sitting on the BSS. However, because of  
912 the larger distances, the required light intensity demands the use of a laser.  
913 This laser<sup>32</sup> is housed in a cylindrical titanium container 705 mm in length  
914 and 170 mm in diameter (Figure 22). Inside the container, an aluminium  
915 inner frame holds the laser and its associated electronics. The laser beam  
916 points upwards and leaves the container through a flat disk diffuser coupled  
917 by bonding to a quartz cylinder ( $n = 1.54$ ). This output window configu-  
918 ration is needed in order to minimize transmission losses due to underwater  
919 sedimentation and biofouling which affect mainly horizontal surfaces. The  
920 actual time of laser emission is obtained from a fast photodiode integrated  
921 into the laser head. Two lines located in a central position in the detector  
922 are equipped with laser beacons.

---

<sup>32</sup>NG-10120-120; Nanolase, presently part of JDS Uniphase Corp., <http://www.jdsu.com>

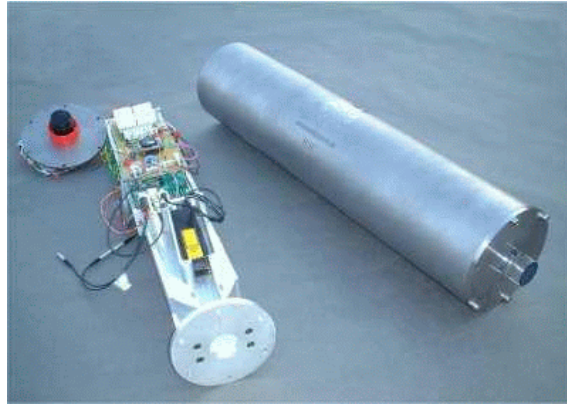


Figure 22: Components of the laser beacon.

923 *3.8. Positioning devices*

924 Each ANTARES detector line is equipped with an acoustic transceiver  
 925 (RxTx module) fixed on its anchor and receiving hydrophones (Rx modules)  
 926 fixed on storeys 1, 8, 14, 19 and 25. There are five Rx modules per line, one  
 927 is placed on the bottom storey and one on the top storey. The others are  
 928 distributed in order to obtain a larger density of hydrophones in the top third  
 929 part of the line, where the maximum curvature of the line shape is expected.  
 930 The RxTx module is composed of a transducer (emitting and receiving hy-  
 931 drophone) placed at the top of a pole on the line anchor and six electronic  
 932 boards (preamplification, CPU, two DSPs, power, emission) integrated in  
 933 the SCM. It emits the acoustic signals in emission mode and acts as an Rx  
 934 module in reception mode. The Rx module is composed of a receiving hy-  
 935 drophone placed on the storey and three electronic boards (preamplification,  
 936 DSP, CPU) included in the LCM. Since the position measurements are based  
 937 on the travel time of acoustic signals, the knowledge of the sound velocity *in*  
 938 *situ* is mandatory: sound velocimeters are distributed on some lines. Data  
 939 from these devices are used to reconstruct by triangulation the positions  
 940 of the hydrophones. In order to obtain the optical modules positions, the  
 941 following complementary information is used:

- 942 • orientation of the OMFs provided by the COMPASS\_MB sitting in each  
 943 LCM;
- 944 • a model for the line shape, see Section 6.4.1.

945 *3.9. Instrumentation line*

946 The instrumentation line has evolved in time from the “MILOM” line  
 947 [15], which was operational from March 2005 to June 2007 to the “IL07” line  
 948 which has been operational since December 2007.

949 This IL07 instrumentation line has six storeys of which three house el-  
 950 ements of the acoustic detection system, which will be described in Sec-  
 951 tion 3.10. The storeys of the line house various oceanographic instruments:  
 952 Acoustic Doppler Current Profilers (ADCP) to monitor the intensity and di-  
 953 rection of the underwater flow; a sound velocimeter to record the local value  
 954 of the sound velocity; probes to measure the conductivity and temperature  
 955 (CT) of the sea water; transmissometers to monitor the light attenuation of  
 956 the water (C-STAR); a dissolved oxygen sensor (O2) widely used by physical  
 957 oceanographers to characterize mixing and ventilation of water masses and  
 958 two cameras continuously connected in order to record images of biolumines-  
 959 cent organisms. A schematic layout of the instruments on the line is shown  
 960 in Figure 23 and details of the instruments are given in Table 3.

Storey	Height above seabed	Device type	Manufacturer	Model	Measured parameters
6	305 m	6 hydrophones	HTI	HTI-90-U	sound level, transients
		CTD	SEABIRD	SBE37-SMP	conductivity, temperature
5	290 m	Optical module	ANTARES	custom	light level
		ADCP	TeledyneRD	Workhorse	sea current velocity
		Camera	AXIS	AXIS221	images
4	210 m	Transmissometer	WETLabs	C-Star	water transparency
		SV	GENISEA/ECA	QUUX-3A(A)	sound velocity
		O <sub>2</sub> probe	AANDERAA	Optode 3830	oxygen level
3	195 m	6 hydrophones	Erlangen	custom	sound level, transients
		CTD	SEABIRD	SBE37-SMP	conductivity, temperature
2	180 m	6 hydrophones	HTI	HTI-90-U	sound level, transients
		Transmissometer	WETLabs	C-Star	water transparency
1	100 m	Optical module	ANTARES	custom	light level
		ADCP	TeledyneRD	Workhorse	sea current velocity
		Camera	AXIS	AXIS221	images
BSS	0 m	pressure sensor	GENISEA/ECA		pressure
		Transponder	IXSEA	RT661B2T	acoustic positioning

Table 3: List of the instruments on the line IL07.

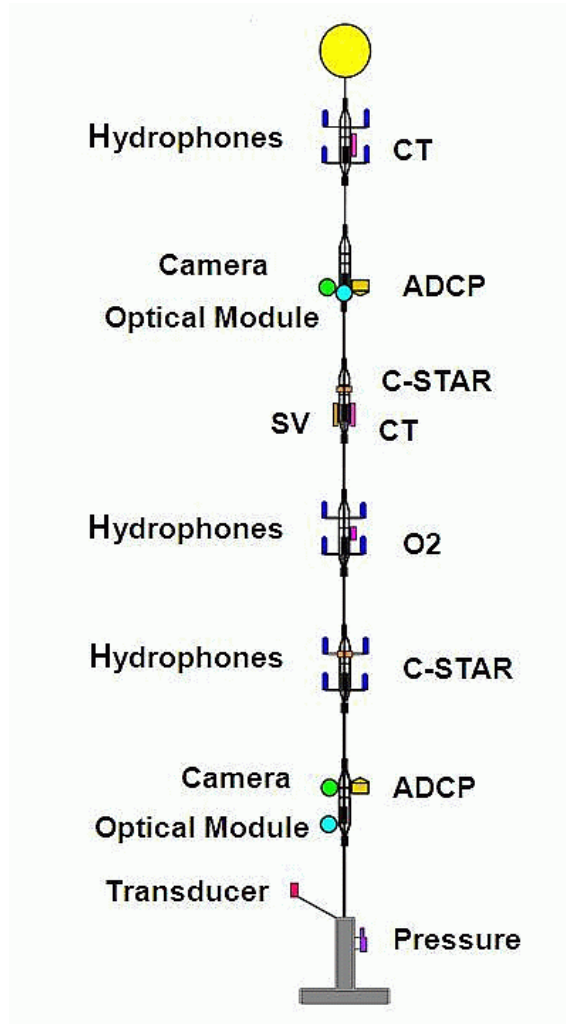


Figure 23: The instrumentation line IL07. Elements are indicated schematically; not drawn to scale.

961 *3.10. Acoustic detection system AMADEUS*

962 The acoustic neutrino detection is integrated into ANTARES in the form  
 963 of Acoustic Storeys (AS) which are modified standard storeys with the PMTs  
 964 replaced by acoustic sensors with custom-designed electronics for signal pro-  
 965 cessing. AMADEUS consists of six ASs, three of them located on the instru-  
 966 mentation line and three on Line 12. Each AS comprises six acoustic sensors  
 967 that are arranged at distances of roughly 1 m from each other. The ASs

968 on the instrumentation line IL07 are located at 180 m, 195 m, and 305 m  
969 above the seabed, respectively. Line 12 is anchored at a horizontal distance  
970 of about 240 m from the IL07, with the ASs positioned at heights of 380 m,  
971 395 m, and 410 m. With this setup, the maximum distance between two ASs  
972 is 340 m.

#### 973 **4. Detector infrastructure**

974 The infrastructure required to power and control the offshore detector  
975 includes the onshore buildings to house the electronics for monitoring and  
976 data acquisition, the main electro-optical cable providing the electrical power  
977 and the data link between the detector and the shore, the junction box and  
978 the interlink cables to distribute the power and the optical fibres to the 13  
979 lines.

##### 980 *4.1. Interlink cable*

981 The connection between the JB and each line is provided by the inter-  
982 link cables. These cables, produced by the ODI company<sup>26</sup>, contain four  
983 monomode optical fibres and two electrical conductors. A complete link be-  
984 tween the JB and a line is composed of three parts: two short cables at each  
985 end (jumpers) and the IL itself as shown in Figure 24. Each jumper is termi-  
986 nated at one end by a penetrator equipped with a water blocking system and  
987 at the other end by a socket fixed on a strong mechanical structure. Whereas  
988 the mounting of the jumpers is performed on shore, the completion of the  
989 connection is realised by a Remotely Operated underwater Vehicle (ROV)  
990 which lays the IL on the seabed, plugs it on the JB side then on the line side.  
991 After each step of the connection operation, both the electrical and optical  
992 contacts are checked from shore to be within specifications.

993 In order to compensate for failures experienced in some of the 16 out-  
994 puts of the JB, interlink cables of a special design are used in the seabed  
995 infrastructure. Each of these special cables connects two separate lines of  
996 the detector with one single JB output. Due to their particular shape, these  
997 cables are denoted as “Y” links. In this configuration, the cable coming from  
998 the JB is split and then linked to the two lines with the same system that is  
999 used for the other lines. The two connected lines share the power provided by  
1000 the JB output. Their DWDM systems are tuned on two different frequency  
1001 domains. The splitting of the electrical conductors and the splicing of the

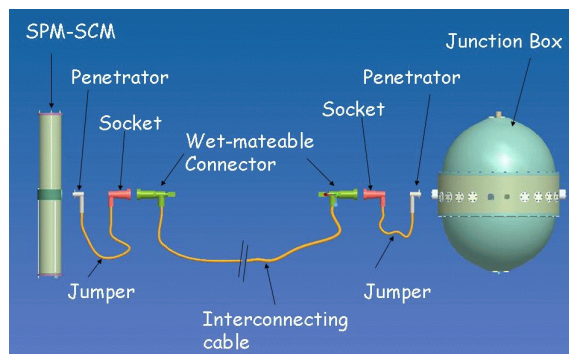


Figure 24: A schematic view of the complete link between the SPM/SCM container of a line and the JB container.

1002 optical fibres are performed in a titanium container located at the end of the  
 1003 common path, at 10 m distance from the JB.

#### 1004 4.2. Junction box

1005 The JB is a pressure resistant titanium container mounted to the JB  
 1006 Frame (JBF). The JB and JBF provide the following facilities:

- 1007 ● connection of the MEOC and of the sea return power electrode;
- 1008 ● power transformer housing;
- 1009 ● line over-current protection system;
- 1010 ● remote diagnostic system;
- 1011 ● 16 electro-optical sockets to plug the interlink cables.

##### 1012 4.2.1. Junction box mechanical layout

1013 The junction box structure, illustrated in Figure 25, is based on a 1 m  
 1014 diameter titanium pressure sphere,

1015 whose hemispheres are separated by a central titanium cylinder (“belt”)  
 1016 through which all power and data connections pass to the exterior. The junc-  
 1017 tion box internal pressure is 1 bar, the external water pressure is  $\approx 250$  bars.  
 1018 Each hemisphere is sealed to the belt with two concentric O-rings. The lower  
 1019 hemisphere contains a transformer immersed in oil<sup>33</sup>, the upper hemisphere

---

<sup>33</sup>Nynas 10GBN naphthalene based transformer oil, meeting ASTM spec D3487 type 1; Nynas AB, <http://www.nynas.com>



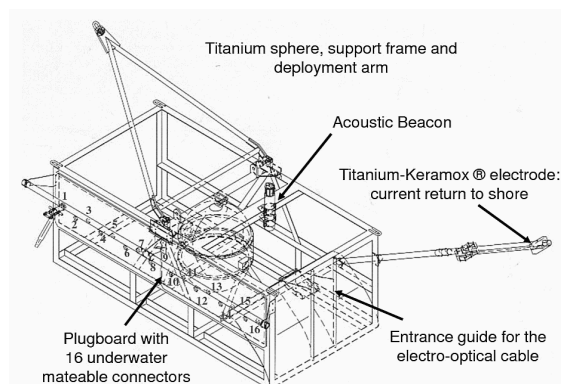


Figure 25: The junction box container and its support frame.

1020 contains the power system slow control electronics. Following component  
 1021 installation, the junction box sphere was qualified in a 24 hour pressure test  
 1022 at 310 bar (20 % overpressure) in a 2.5 m diameter caisson<sup>10</sup>.

1023 The sphere is supported within a rectangular titanium transit frame. The  
 1024 cage incorporates an acoustic transponder to allow triangulation of the junc-  
 1025 tion box position during deployment, an electrode for the return of the cur-  
 1026 rent to shore, and an entry guide to protect the undersea cable from scuffing  
 1027 during the deployment procedure and bending too sharply. In addition, it  
 1028 is equipped with a plug board with 16 deep sea wet mateable electro-optical  
 1029 sockets for the interlink cable connections. Figure 26 shows the junction  
 1030 box on the deck of the deployment ship. The sphere, the cable penetrations  
 1031 through the belt and the plug board of wet-mateable connectors are visible.

1032

#### 1033 4.2.2. Junction box cabling

1034 The junction box is equipped with 16 outputs for connection of the de-  
 1035 tection and instrumentation lines. The typical power drawn for a detection  
 1036 line is around 1 kW. The junction box outputs are galvanically separated  
 1037 through a transformer with 16 individual secondaries rated at 500 V. Two  
 1038 additional windings rated at 240 V power the junction box internal slow  
 1039 control systems. Each output is protected by a thermo-magnetic breaker<sup>34</sup>  
 1040 set to a 5 A threshold. In addition, each breaker can be rearmed or opened

<sup>34</sup>PKZ2/ZN6 with RE-PZK2 remote control block; Moeller, <http://www.moeller.fr>



Figure 26: Junction box on the deck of the deployment ship.

1041 by remote control (Figure 27) should the leakage current monitored by an  
1042 inductive current sensor<sup>35</sup> exceed a safe threshold. Each output has four  
1043 optical fibres: one pair used for data up- and down-links and the other for  
1044 duplicated distribution of the central clock pulse train. In addition, each out-  
1045 put contains a pair of electrical conductors providing AC power in the range  
1046 435-480 V. The conductors and optical fibres of unmated output connectors  
1047 are protected from sea water exposure by a shutter which opens only during  
1048 the final phase of cable insertion. Breakers corresponding to unused outputs  
1049 are kept in the closed (powered) position, both to minimize the number of  
1050 output breaker operations and to allow early detection of water infiltration  
1051 past the shutter of a connector, which would be manifested as an increase in  
1052 leakage current monitored on the corresponding current sensor. Breaker ma-  
1053 nipulation is possible with any of three independent control channels through  
1054 the wired-OR powering of intermediate 240 V relays.

#### 1055 *4.2.3. Junction box slow control electronics*

1056 Output breaker manipulation and measurement of currents, temperatures  
1057 and humidity are the main activities of the triply redundant junction box slow  
1058 control system. The system uses eight of the 48 fibres in the undersea cable  
1059 and is based on three control cards built in two different technologies.

---

<sup>35</sup>“MACC plus” Zero flux current transformer, 10 A full scale, 100  $\mu$ A resolution; Hitec BV, <http://www.hitecups.com>

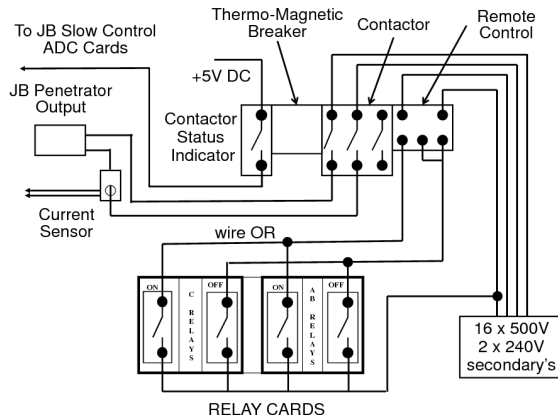


Figure 27: Junction box output breaker management.

1060 In the first of these, two identical cards communicate with the shore sta-  
 1061 tion through  $160 \text{ Mb s}^{-1}$  links, using a transmitter/receiver chip set<sup>36</sup> with  
 1062 the Photon Techno PT5543-13-3-SC laser emitter and PT6143-155-SC re-  
 1063 ceiver operating at 1550 nm. Associated firmware is embedded in FPGAs<sup>37</sup>.  
 1064 Each card can simultaneously stream 16-bit digitized data from 48 inter-  
 1065 nal temperature and humidity sensors, and 24-bit data at 2.6 kHz sampling  
 1066 from a group of 4 “MACC plus” inductive current sensors. This latter data  
 1067 is passed onshore to a DSP<sup>38</sup> and used for sinusoid reconstruction and RMS  
 1068 current calculation. A third card, designed for ultra-low power operation and  
 1069 powered by lithium batteries<sup>39</sup>, is based on a microcontroller<sup>40</sup> with 60 kbyte  
 1070 flash and 2048 byte RAM memory equipped with eight 12-bit ADC entries  
 1071 and 45 digital I/O ports. This card communicates, even in case of JB power  
 1072 failure, at very low speed (1200 Baud) using an NDL7701 laser uplink oper-  
 1073 ating at 1550nm and an LPD80 pin diode receiver. This channel has a power  
 1074 consumption of  $5 \mu\text{A}$  in sleep mode and  $60 \mu\text{A}$  when active. When the uplink  
 1075 is transmitting, the maximum power consumption of the card is 100 mA for  
 1076 short periods.

1077 A hermetic stainless steel diaphragm separates the lower transformer com-

<sup>36</sup>HDMP-1022/1024; Agilent Technologies Inc., <http://www.agilent.com>

<sup>37</sup>7256S; Altera Corp., <http://www.altera.com>

<sup>38</sup>TMS320C5510 200 MHz; Texas Instruments, <http://www.ti.com>

<sup>39</sup>Eight SAFT LSH20 Lithium elements of 3.6 V, 13 Ah each.

<sup>40</sup>MSP430F149; Texas Instruments, <http://www.ti.com>

1078 partment from the hemisphere containing the slow control system and fibre  
1079 optic routing devices. The electronics is mounted on an aluminium heat  
1080 sink disk (Figure 28) making thermal contact with the titanium belt of the  
junction box. The diaphragm and heat spreader disk sandwich a thermal

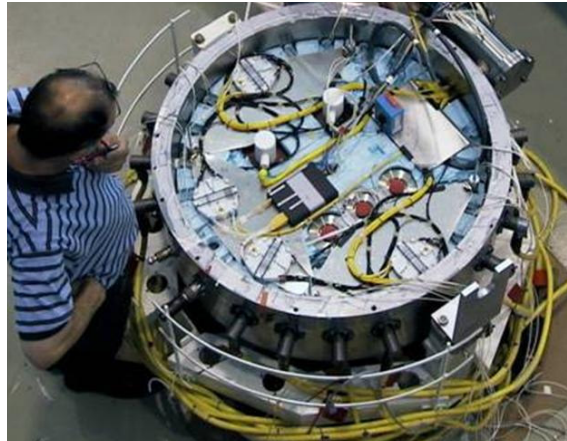


Figure 28: View inside the open JB: heat-spreader disk, transformer connections and primary circuit current sensor, passive fibre optic splitters and cassettes protecting fibre fusion splices.

1081 insulation blanket of silica aerogel<sup>41</sup> which also serves as a getter for water  
1082 vapour.  
1083

#### 1084 *4.2.4. Fibre optic signal distribution in the junction box*

1085 Each junction box output connector contains four optical fibres with the  
1086 following functions:

- 1087 • DAQ Rx<sub>n</sub> (data downlink from shore; n=1→16);
- 1088 • DAQ Tx<sub>n</sub> (data uplink to shore; n=1→16);
- 1089 • Clock channel A;
- 1090 • Clock channel B.

1091 DAQ Tx and Rx are specific to each line, and are accommodated using 32  
1092 fibres in the undersea cable, which are point-to-point spliced in the junction  
1093 box hub to their respective fibres in the 16 output connectors.

---

<sup>41</sup>Spaceloft<sup>®</sup>; Aspen Aerogels Inc., <http://www.aerogel.com>

1094 The central clock signal, vital for time referencing of photomultiplier data  
1095 to subnanosecond precision, is transmitted with a 4-fold redundancy. Pulse  
1096 trains from two independent, identical clock transmitters at the shore station  
1097 are split for broadcast on four undersea fibres. In the junction box they are  
1098 routed via dual-input 16-way passive splitters so that clock pulse trains from  
1099 either or both transmitters are available on every output connector. All  
1100 internal fibre connections are made by fusion splicing, resulting in an optical  
1101 loss of around 0.01 dB per joint. The laser diode intensity in the shore based  
1102 clock system is sufficient to maintain an optical power margin of 12 dB over  
1103 the attenuation in the undersea cable and passive splitters.

#### 1104 *4.3. Main electro-optical cable*

1105 The main electro-optical cable provides the electrical power link and the  
1106 optical data link between the shore station and the detector. The selected  
1107 cable, a standard telecommunications type, satisfies the electrical and optical  
1108 transmission specifications as well as the environmental and mechanical cri-  
1109 teria such as temperature tolerance, bending radius and mechanical strength.

##### 1110 *4.3.1. Cable*

1111 Prior to deployment of the MEOC, surveys by a ROV have been carried  
1112 out to select the best possible offshore site for the apparatus in terms of  
1113 flatness of the sea bottom and the absence of obstacles. The MEOC has  
1114 been deployed from the site to the shore by a specialized cable-laying ship  
1115 and crew under the responsibility of Alcatel. The cable was tested for op-  
1116 tical and power transmission prior to the deployment operation. Figure 29  
1117 shows the structure of the different cable sections used at different depths  
1118 and Table 4 gives the main characteristics of the undersea cable<sup>42</sup>, which con-  
1119 tains 48 monomode optical fibres<sup>43</sup> in a stainless steel tube surrounded by  
1120 a “pressure vault” of two windings of steel armour wires. A tubular copper  
1121 power conductor surrounds the vault and delivers current up to a maximum  
1122 of 10 A to the junction box. A standard undersea cable configuration with a  
1123 single conductor (normally used for series powering of repeaters in long-haul  
1124 cables) was chosen to minimize the cable cost and weight. The use of the sea  
1125 for current return reduces ohmic losses by a factor 4 compared with a cable  
1126 sharing equivalent cross-section between supply and return conductors.

---

<sup>42</sup>Alcatel URC3 Type 4 (unrepeatered); Alcatel-Lucent, <http://www.alcatel-lucent.com>

<sup>43</sup>Type G24B DE 1302XB (BBO) WB B1,  $\varnothing = 125 \mu\text{m}$ .



Figure 29: Sections of the undersea cable.

Electrical resistance	$1 \Omega \text{ km}^{-1}$
Fibre attenuation	$0.18 \text{ dB km}^{-1}$
Fibre chromatic dispersion	$21 \text{ ps nm}^{-1} \text{ km}^{-1}$

Table 4: Characteristics of the undersea cable.

1127 On the deep, smooth seabed the cable exterior terminates in a 21 mm  
 1128 diameter polyethylene sheath (“Light-Weight” configuration). An additional  
 1129 polypropylene jacket (LWP) protects the cable in the zone of shelving seabed.  
 1130 In shallower water with risk of damage from fishing or boat anchors, the cable  
 1131 has an additional single layer of armour wires (SA) and a coating of tarred  
 1132 polyurethane yarn. The final short section in very shallow water has an  
 1133 additional armour layer (DA). This sequence with cable sections lengths and  
 1134 water depths is summarized in Table 5. On the sea side, the cable terminates  
 1135 in a titanium shell dry-mated electro-optical connector<sup>44</sup> (Figure 30) mating  
 1136 with a receptacle in the junction box belt. The overall weight of the deployed  
 1137 cable is 88 tons for a total length of 41.3 km.

1138 The central electrical conductor connects with the HV pole of the primary  
 1139 winding of the junction box transformer. The LV pole returns the current  
 1140 through an external sea electrode<sup>45</sup> to the power hut, which has receiving

<sup>44</sup>SeaCon Europe Ltd, <http://www.seaconbrantner.com>

<sup>45</sup>Titanium with Keramox<sup>®</sup> coating, of length 1.6 m and diameter 40 mm; Magneto

<b>LW</b> 'Light-Weight'	Length	17.4 km
	Depth	> 2300 m
<b>LWP</b> 'LW-Protected'	Length	10.2 km
	Depth	422 to 2300 m
<b>SA</b> 'Single Armoured'	Length	12.1 km
	Depth	27 to 422 m
<b>DA</b> 'Double Armoured'	Length	1.6 km
	Depth	< 27 m

Table 5: Layout of the undersea cable.



Figure 30: Electro-optical plug and receptacle for connection of the undersea cable to the junction box.

1141 electrodes buried in the nearby ground.

#### 1142 4.3.2. Power supply to the junction box

1143 Figure 31 illustrates the power system of the detector up to the outputs  
 1144 of the junction box. The detector shore power supply draws 400 V 50 Hz  
 1145 AC power from the electricity grid. The power supply located in a build-  
 1146 ing (the Power Hut) near the cable landing beach raises the voltage to the  
 1147 range 3700-4100 V for passage through the undersea cable to the junction

---

BV, <http://www.magneto.nl>

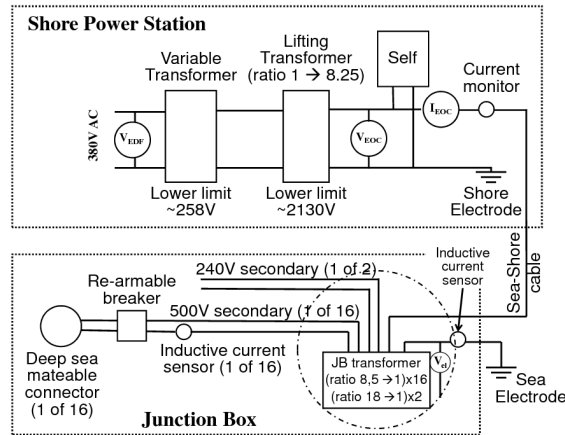


Figure 31: Power distribution system from the shore to the underwater junction box.

1148 box. The voltage at the cable input is adjusted using a motor driven variable  
 1149 transformer, depending on the load requirement (i.e. the number of lines to  
 1150 be powered). The 50 Hz AC power system was chosen as the best compromise  
 1151 for power delivery over the 42 km transmission length. Although direct  
 1152 and indirect losses are increased relative to a DC system having the same  
 1153 voltage and current limits, the AC option was preferred since it allows for  
 1154 more reliable variation of the cable entry voltage, using passive (transformer)  
 1155 elements. It also has a greater simplicity and reliability at the seabed distri-  
 1156 bution node through the use of a transformer with multiple windings in the  
 1157 junction box. The  $9 \mu\text{F}$  cable capacitance needs to be compensated; this is  
 1158 largely achieved through the use of a 1.4 H self inductance at the shore  
 1159 end of the cable. The self inductance strongly reduces the reactive component  
 1160 produced by the cable capacitance. The dissipation in the cable is there-  
 1161 fore mostly resistive and corresponds to about 10% of the 36 kW (9.6 A at  
 1162 3800 V) leaving the shore station.

#### 1163 4.4. Shore facilities

1164 The onshore infrastructure consists of two separate buildings, the Shore  
 1165 Station housing control and data management infrastructure and providing  
 1166 space for onsite personnel, and the Power Hut devoted to power distribution  
 1167 requirements. The shore station is situated at La Seyne-sur-Mer.

1168 The building has three rooms dedicated to the operation of the ANTARES  
 1169 experiment: a computer room, a control room, and a service room. The



1170 computer room hosts the racks for the clock crate, the 13 onshore DWDM  
1171 crates (counterparts of the DWDM boards of the 13 lines) and the PC farm  
1172 for data filtering and storage. The control room contains various computers  
1173 for apparatus control and status monitoring.

1174 The Power Hut is located near to the MEOC landing point at Les Sablettes,  
1175 and is connected to the latter with a fibre optical link 1.5 km long. The  
1176 Power Hut is connected to the 60 kVA, 400 V three-phase electrical distribu-  
1177 tion from Électricité de France. The building has been adapted to house the  
1178 transformer 400/4000 V, the MEOC to shore link rack as well as the return  
1179 current electrodes.

## 1180 5. Construction

### 1181 5.1. Generalities

1182 The construction of the apparatus started in 2001 with the installation of  
1183 the long distance electro-optical cable. In late 2002 the underwater junction  
1184 box was installed; the deep sea end of the cable was recovered for this purpose,  
1185 the junction box dry connected to it, tested on the deck of the ship and finally  
1186 deployed. During the following years several prototype lines were installed  
1187 and operated *in situ*, allowing the validation and optimization of their design,  
1188 as well as the evaluation of possible long-term effects. The first detection line  
1189 was installed in early 2006 and the last two lines of the apparatus were put  
1190 into operation in May 2008. A European-wide effort was mobilized for the  
1191 construction of the detector. While all optical modules were assembled in just  
1192 one laboratory, the production of different mechanical parts and electronics  
1193 boards was performed by a number of laboratories in different countries.  
1194 A large effort was subsequently devoted to the assembly of the electronics  
1195 modules and of the complete lines. Three sites fabricated electronics modules  
1196 in order to feed two laboratories which worked independently on the assembly  
1197 of new lines. When running at full speed, two lines were produced every three  
1198 months.

1199 Since the same integration tasks had to be performed at different sites,  
1200 special care was devoted to the development of dedicated tools, the definition  
1201 of detailed procedures and the distribution of the expertise among the differ-  
1202 ent teams, under a unified Quality Control approach. A coherent scenario of  
1203 tests to be performed at the different integration levels made it possible to  
1204 identify faulty components in order to avoid delays in the integration of the

1205 lines. Logistics was an important issue; the Cellule Logistique of IN2P3<sup>46</sup>  
1206 was used for managing the transportations.

### 1207 *5.2. Quality assurance and quality control*

1208 The organization of the Quality Assurance/Quality Control activities was  
1209 based on the methodologies defined by the rules of ISO 9001:2000<sup>47</sup>, with an  
1210 effort to guarantee a high level of adaptability and flexibility. A special  
1211 attention was given to defining rules for proper management of the docu-  
1212 mentation, with different levels of approval established for the most critical  
1213 documents, such as the integration and test procedures. All documents were  
1214 stored in a centralised repository, accessible through a password-protected  
1215 website. Problems and changes in the organization were traced through ap-  
1216 propriate documents: a Non-Conformity Report was the tool used to report  
1217 the problems found at all levels in the construction of the apparatus. Im-  
1218 provements of the organization were sometimes defined after the treatment  
1219 of such reports, and implemented in response to a Design Change Request.

1220 A key document for the construction of the apparatus was the Risk Anal-  
1221 ysis, whose output of served as the basis, first for the implementation of  
1222 detailed prototyping campaigns and later for the definition of the test cri-  
1223 teria to be adopted during the construction of the apparatus. A general  
1224 Quality Plan was then put in place, defining the main guidelines for Qual-  
1225 ity management in the Collaboration, and all laboratories participating in  
1226 the construction of the apparatus were required to define their local Quality  
1227 Plans, to be applied under the control of Local Quality Supervisors. A Qual-  
1228 ity Plan was also required from the external providers at the time of placing  
1229 the orders. A program of audit activities was also set up for all laboratories  
1230 in order to continually improve the system.

1231 A central database was used for collecting traceability information and,  
1232 when applicable, calibration data of all products, which were individually  
1233 identified by a bar-code label built according to a well defined Product Break-  
1234 down Structure of the apparatus and a serial number. Detailed information  
1235 of which products were integrated in which parts of the apparatus was also  
1236 stored in this DB, so that all necessary information for the configuration of  
1237 the apparatus at the time of operation was immediately available.

---

<sup>46</sup>ULISSE, <http://ulisse.in2p3.fr>

<sup>47</sup>[http://www.iso.org/iso/catalogue\\_detail?csnumber=21823](http://www.iso.org/iso/catalogue_detail?csnumber=21823)

1238 *5.3. Assembly*

1239 *5.3.1. Control module integration*

1240 Construction of the electronics modules required a very high level of reli-  
1241 ability since the failure of one module could lead to the loss of functionality  
1242 of a whole sector of a line.

1243 The integration of the electronics modules was a delicate task because  
1244 of the design of the mechanical crate, the fact that electronics boards were  
1245 densely packed inside it and the need to have careful handling of optical fibres  
1246 at all times. Detailed procedures were therefore defined and dedicated tools  
1247 developed. A full functionality test was performed on all integrated modules  
1248 in order to find and cure all possible problems. Calibration of the front-end  
1249 electronics was also performed during these tests.

1250 *5.3.2. Line integration*

1251 Line integration took place at two different sites. The sharing of expertise,  
1252 the usage of the same tools and procedures and the respect of quality rules  
1253 ensured that the level of quality was the same in the two laboratories. This  
1254 was confirmed by a cross calibration between the two sites. The lines were  
1255 integrated from the bottom to the top. Optical splices were used on all optical  
1256 fibre connections for maximum reliability. Once a sector was completed,  
1257 a calibration in a dedicated dark room (or in dark boxes) for the optical  
1258 modules was performed. Simultaneously, the integration of a new sector  
1259 started. The purpose of the tests in the dark room was to verify the full  
1260 functionality of the sector, as well as to provide an initial time and charge  
1261 calibration for all optical modules in the final configuration of the line. A  
1262 calibration of the tiltmeters in each storey was also performed. Then, the  
1263 storeys were arranged on a line transportation pallet. The optical modules  
1264 were temporarily connected to their storeys for the tests, but were then  
1265 removed and transported separately from the line for maximum safety.

1266 *5.3.3. Deployment preparation*

1267 The final steps of integration took place in a dedicated hangar at the  
1268 port of La Seyne-sur-Mer. Here, a final functionality test of the lines was  
1269 performed. Then, in preparation for deployment, the storeys were arranged  
1270 on wheeled carts, equipped with the optical modules and the instrumenta-  
1271 tion and moved onto a deployment pallet. The top buoy and the bottom  
1272 deadweight were finally added. An integrated line was arranged on a single  
1273 pallet which was then installed on the deck of the ship for the deployment.

1274 *5.4. Line deployments and connections*

1275 The vessel Castor of the Foselev Marine Company was used for installa-  
1276 tion of all ANTARES lines.

1277 The deployment of a line proceeds as follows: once the ship reaches the  
1278 site, the first package to be launched under the boat frame winch is the  
1279 heavy BSS. Then, the storeys are put into the water one by one until the  
1280 top buoy of the line. Two 5-ton winches are used on the deployment ship,  
1281 each equipped with a specially designed remote release hook which made it  
1282 possible to avoid the use of divers during the deployment. Once the top  
1283 buoy is in water it is connected to the deep sea cable winch through a hook  
1284 equipped with an acoustic release. The transponders mounted on the BSS  
1285 are localized while paying out cable until the seabed is reached. The ship  
1286 then adjusts its position using its Dynamic Positioning (DP) capabilities in  
1287 order to place the BSS on the target location. This procedure allows the  
1288 positioning of the lines within a few metres from their target points.

1289 A team of 12 people from the Collaboration is needed for a line deploy-  
1290 ment in addition to the 4 deck crew. The typical duration of activities on site,  
1291 including DP station tests, acoustic position tests, launch and deployment of  
1292 the line and cable recovery is about 8 hours.

1293 As explained previously, the connection between the junction box and  
1294 the lines is made with electro-optical cables of suitable length (ranging from  
1295 120 to 350 m), equipped with a wet-mateable connector at each end. These  
1296 interlink cables are prepared on turrets which are deposited on the seabed,  
1297 either being deployed with the deep sea cable winch or in free falling mode.  
1298 An underwater vehicle is then used for the subsequent actions: it moves the  
1299 turret close to the JB and connects one end of the cable to a free output of  
1300 the JB. Once a good connection is established at the level of the junction  
1301 box, the underwater vehicle moves the turret towards the base of the line to  
1302 be connected, while routing the cable on the seabed. Finally, the connection  
1303 to the BSS is performed. Each operation is monitored from the shore station  
1304 where tests are made in order to test electrical and optical continuity.

1305 All connection operations were performed by means of the ROV Victor of  
1306 IFREMER, except the connection of the second line of the apparatus which  
1307 was performed with the manned submersible Nautille of IFREMER.

1308 The weather conditions permitting the safe operation of an underwater

1309 vehicle depend on the support vessel used. Wind limits of 20 knots<sup>48</sup> were  
1310 found when Victor was operated onboard Castor, while larger vessels allowed  
1311 operation with winds up to around 35 kts. The seabed conditions have also  
1312 to be acceptable, since operation of the ROV becomes difficult when the sea  
1313 current exceeds  $10 \text{ cm s}^{-1}$ .

1314 The ROV was also used during the detector construction for other tasks,  
1315 such as:

- 1316 • inspection and test of the outputs of the junction box;
- 1317 • survey of optical modules;
- 1318 • deployment of the seismograph;
- 1319 • measurement of the electrical current and visual survey of the MEOC;
- 1320 • survey of the acoustic transponders installed around the apparatus;
- 1321 • change of the interlink cables.

### 1322 5.5. Maintenance

1323 A simplified scheme of the construction organization is still operating  
1324 today for maintenance of the apparatus. The possibility of recovering lines is  
1325 foreseen in case of severe functionality problems while no routine maintenance  
1326 of the offshore apparatus is scheduled. A recovery operation is performed as  
1327 follows: once the ship is on site, the hook holding the BSS to its deadweight  
1328 is opened by means of a release command issued acoustically from onboard.  
1329 Once the deadweight is released, the line comes up to the surface freely in  
1330 about 40 minutes. In order to perform this operation safely, the sea current  
1331 conditions must be suitable with deep sea currents not exceeding  $5 \text{ cm s}^{-1}$   
1332 in order to prevent the released line from colliding with the other lines of the  
1333 detector. When the top buoy of the line reaches the surface, it is dragged  
1334 to the ship. Then, the recovery of the rest of the line takes place in a way  
1335 similar to a reversed deployment procedure.

1336 A set of spare components for all different products is available, so that  
1337 generally the lines could be repaired without delays for new productions of  
1338 elements. The different laboratories remain, however, in charge of the prod-  
1339 ucts they have originally provided, in case new productions must be launched,  
1340 so components would be provided with the same quality level as during the

---

<sup>48</sup>1 knot =  $1.852 \text{ km h}^{-1}$ .

1341 construction. One laboratory is still active for assembly of new electronics  
1342 modules while another laboratory is still active for line dismantling and re-  
1343 integration. A line recovery gives also the opportunity to inspect all parts of  
1344 the lines for any effects induced by the long-term operation at large depth.

## 1345 **6. Operation**

### 1346 *6.1. Apparatus control*

1347 Control of the apparatus is performed from the shore station in Institute  
1348 Michel Pacha, which is manned during the day for this purpose, although full  
1349 control can also be performed remotely from all institutes participating in the  
1350 experiment by means of a VNC (Virtual Network Computing) application<sup>49</sup>.  
1351 All information for apparatus control is stored in the central database of the  
1352 experiment, located together with the resources for mass storage of data at  
1353 the IN2P3 Centre de Calcul in Lyon<sup>50</sup>. The Oracle database is also regularly  
1354 updated with the slow control information from the data acquisition system  
1355 so as to maintain a detailed record of the performance of each element of the  
1356 apparatus.

1357 The operator controls the data acquisition operations by means of two  
1358 main programs, both provided with a Graphical User Interface (GUI), one for  
1359 monitoring and control of the power delivery system, and the second one for  
1360 control of the data acquisition. The former program is capable of delivering  
1361 the commands set by the operator to the onshore power system facility or  
1362 directly to the junction box, as appropriate. It can also be used to retrieve  
1363 monitoring data from all sensors of the junction box. The sensor data are  
1364 converted into engineering units for on-screen presentation and are written  
1365 at regular intervals into the database. The environmental conditions inside  
1366 the power distribution hut are also monitored and recorded regularly. Alarm  
1367 thresholds are set for each sensor in the database so as to define different  
1368 levels, and priorities, of alarms: low priority alarms alert the operator with  
1369 on-screen messages while higher priority alarms can also generate SMS text  
1370 messages, and depending on the criticality of the sensor, may trigger a power  
1371 shutdown after a predetermined delay.

1372 In total, the data acquisition control system involves about 750 processes  
1373 (300 offshore processes for data acquisition, 300 offshore processes for slow

---

<sup>49</sup><http://www.realvnc.com>

<sup>50</sup><http://cc.in2p3.fr>

1374 control, and about 120 processes running on the onshore computers for data  
1375 processing and filtering, monitoring and user interface). These processes  
1376 implement the same state machine diagram [8]. Transitions between dif-  
1377 ferent states are decided by the operator and handled by the main control  
1378 GUI. All relevant configuration information is extracted from the database.  
1379 A message logging system keeps track of all operations in a designated file  
1380 (that is archived regularly); warnings generated by any process are captured,  
1381 recorded in the same file and shown on the computer screen for operator  
1382 alert. In order to archive data efficiently, the main control GUI updates the  
1383 run number regularly. The database system is also used to keep track of  
1384 the history of the detector integration and the data taking. A number of  
1385 monitoring programs have been developed to monitor different data com-  
1386 ing from the apparatus so that the operator can have a detailed view of  
1387 the working conditions in the apparatus at a glance; this is very important  
1388 for an undersea apparatus, since depending on the optical background con-  
1389 ditions, the user has to choose the best data taking configuration in order  
1390 to maximise the data quality. Monitored quantities include environmental  
1391 conditions inside the electronics modules (temperature, humidity), position  
1392 information retrieved by the compasses and tiltmeters inside the electronics  
1393 modules, PMT hit rates, the measured sea current direction and speed. A  
1394 fraction of the data is reconstructed online and reconstructed events are also  
1395 displayed.

## 1396 *6.2. Data acquisition*

1397 The operations onshore are optimized so as to maximize the time devoted  
1398 to data taking. The data collected offshore are temporarily stored in high  
1399 capacity buffers on the LCMs which allow a de-randomisation of the data  
1400 flow. The data are packed offshore as arrays of hits of predefined time frame  
1401 duration of about 100 ms. Depending on the hit rate of the PMTs, the size  
1402 of these data packets amounts to 60–200 kB. The data are then sent to shore  
1403 in such a way that the data collected for the full detector for the same time  
1404 frame are sent to a single data filter process in the onshore data processing  
1405 system. The data flow to the different data filter processes is staggered to  
1406 avoid network congestion.

1407 The onshore data processing system consists of about 50 PCs running  
1408 the GNU/Linux operating system. To make optimal use of the multi-core  
1409 technology, four data filter processes run on each PC. The physics events  
1410 are filtered from the data by the data filter process using a fast algorithm,

1411 as described in the next subsection. For one processor, the typical time  
 1412 needed to process 100 ms of raw data amounts to 500 ms. The available time  
 1413 allows the application of concurrent software triggers to the same data. On  
 1414 average, the data flow is reduced by a factor of about 10,000. The filtered  
 1415 data are written to disk in ROOT<sup>51</sup> format by a central data writing process  
 1416 and copied every night to the computer centre in Lyon. The count rate  
 1417 information of every PMT is stored together with the physics data. The  
 1418 sampling frequency of these rate measurements is about 10 Hz.

1419 The data from the readout of the various instruments are transferred as  
 1420 an array of parameter values and stored in the database via a single process.  
 1421 The readout of the various deep sea instruments is scheduled via read requests  
 1422 that are sent from shore by a designated process. The frequency of these read  
 1423 requests is defined in the database. A general purpose data server based on  
 1424 the tagged data concept is used to route messages and data [16]. For instance,  
 1425 there is one such server to route the physics events to the data writer which  
 1426 is also used for online monitoring.

### 1427 *6.3. Trigger*

1428 The data filter algorithm applied onshore is based on different trigger  
 1429 criteria, including a general purpose muon trigger, a directional trigger, muon  
 1430 triggers based on local coincidences, a minimum bias trigger for monitoring  
 1431 the data quality, and dedicated triggers for multi-messenger investigations.

1432 The general purpose (“standard”) muon trigger makes use of the general  
 1433 causality relation:

$$|t_i - t_j| \leq r_{ij} \times \frac{n}{c} \quad (2)$$

1434 where  $t_i$  ( $t_j$ ) refers to the time of hit  $i$  ( $j$ ),  $r_{ij}$  to the distance between PMTs  
 1435  $i$  and  $j$ ,  $c$  is the speed of light and  $n$  the index of refraction of the sea water  
 1436 (Figure 32, left). The direction of the muon, and hence of the neutrino,  
 1437 being not used, this trigger is sensitive to muons covering the full sky. To  
 1438 limit the rate of accidental correlations (i.e. to increase the purity of the  
 1439 event samples), the hits have to be preselected. This preselection provides  
 1440 the L1 signals, i.e. either coincidences in a time window of 20 ns between  
 1441 two neighbouring PMTs in the same storey or the occurrence of large pulses

---

<sup>51</sup><http://root.cern.ch>



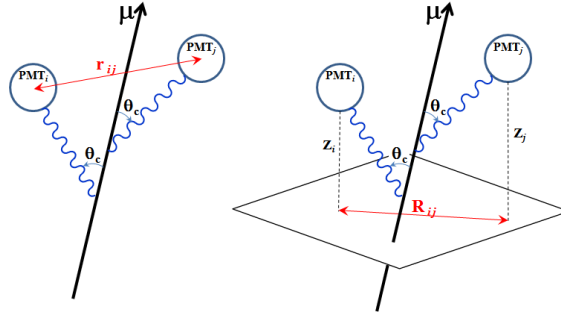


Figure 32: Definitions of the symbols used in equation 2 (left) and in equation 3 (right).

1442 (number of photoelectrons typically greater than 3 in a single PMT). Then,  
 1443 the trigger criteria consist either in a set of at least 5 L1 hits that are causally  
 1444 related or in a local cluster of neighbouring L1 hits. The efficiency and  
 1445 the purity of this trigger have been determined with a simulation of the  
 1446 detector response to muons and accounting for the observed background [8].  
 1447 The efficiency grows fast above 10 detected photons and reaches  $\approx 1$  at  
 1448 40 detected photons. The typical threshold for the neutrino energy is a few  
 1449 hundred GeV. The purity is of the order of 90%, the remaining impurity being  
 1450 mainly due to (low-energy) muons which in combination with the random  
 1451 background produce a trigger; only a small fraction of the events ( $\ll 1\%$ )  
 1452 is found to be due to accidental correlations. The observed trigger rate is  
 1453 thus dominated by the background of atmospheric muons and amounts to  
 1454 5–10 Hz (depending on the trigger conditions). The standard trigger can  
 1455 operate with hit rates in each PMT up to about 250 kHz.

1456 In addition to the standard trigger, a directional trigger has been imple-  
 1457 mented to maximize the detection efficiency of tracks coming from predefined  
 1458 directions. Currently, this trigger is used to look for events coming from the  
 1459 Galactic centre. This trigger makes use of the following direction specific  
 1460 causality relation:

$$\begin{aligned}
 & (z_i - z_j) - R_{ij} \tan \theta_C \\
 & \leq c(t_i - t_j) \leq (z_i - z_j) + R_{ij} \tan \theta_C
 \end{aligned} \tag{3}$$

1461 where  $z_i$  refers to the position of hit  $i$  along the neutrino direction,  $R_{ij}$   
 1462 refers to distance between the positions of hits  $i$  and  $j$  in the plane per-  
 1463 pendicular to the neutrino direction and  $\theta_C$  is the Cherenkov angle in water  
 1464 (Figure 32, right). Compared to equation 2, this condition is more stringent

1465 because the 2-dimensional distance  $R_{ij}$  is always smaller than the corre-  
1466 sponding 3-dimensional distance. Furthermore, this distance corresponds to  
1467 the distance travelled by the photon (and not by the muon). Hence, it can  
1468 be limited to several absorption lengths without loss of detection efficiency.  
1469 This restriction reduces the combinatorics significantly. As a consequence,  
1470 all hits can be considered for the directional trigger and not only the prese-  
1471 lected hits used for the standard trigger, without compromising the purity of  
1472 the physics events. In a field of view of about 10 degrees around the selected  
1473 direction and for neutrino energy below 1 TeV, the detection efficiency with  
1474 the directional trigger is 2 times higher than that obtained with the standard  
1475 trigger.

1476 Additional trigger schemes have been implemented to allow multi-messenger  
1477 searches. The onshore data processing system is linked to the Gamma-ray  
1478 bursts Coordinates Network (GCN)<sup>52</sup>. There are about 1 to 2 GCN alerts  
1479 distributed per day and half of them correspond to a real gamma-ray burst.  
1480 For each alert, all raw data are saved to disk during a preset period (presently  
1481 2 minutes). The buffering of the data in the data filter processors is used  
1482 to save the data up to about one minute before the actual alert. Further-  
1483 more, ANTARES is capable of distributing proper event alerts to external  
1484 detectors. A collaboration with the TAROT [17] optical telescope has been  
1485 recently established in this respect. The direction of interesting neutrino  
1486 triggers (two neutrinos within 3 degrees within a time window of 15 minutes  
1487 or a single event of very high energy) are sent to the TAROT telescope in  
1488 Chile in order that a series of optical follow-up images can be taken. Such  
1489 procedures are well-suited to maximize the sensitivity for transient sources  
1490 such as gamma-ray bursters or flaring sources.

## 1491 *6.4. Calibration*

### 1492 *6.4.1. Position determination*

1493 Accurate position information for each OM is needed for good event re-  
1494 construction (cf. Section 2.2.4). The shape of each line is reconstructed by  
1495 performing a fit based on all the available measurements: positions coming  
1496 from the acoustic positioning system, headings provided by the compasses  
1497 and tilt angles provided by the tiltmeters. These measurements are per-  
1498 formed every two minutes. The relative positions of the OMs are then de-

---

<sup>52</sup><http://gcn.gsfc.nasa.gov/>

1499 duced from the reconstructed line shape and from the known geometry of the  
1500 storeys: a hydrophone is mounted on a storey offset from the centre of the  
1501 storey. The acoustic positioning system described below allows to determine  
1502 the position of the hydrophone. Combining the hydrophone position with  
1503 the tilt and heading information of the same storey one obtains the position  
1504 and the orientation of that storey. Five storeys of a line are equipped with  
1505 hydrophones. From the position and orientation of these five storeys and  
1506 from the tilt and heading measured in the other storeys, the shape of the  
1507 line can be reconstructed and the position of every OM can be determined.

1508 The reconstruction of the line shape is based on a model which predicts  
1509 the mechanical behaviour of the line under the influence of the sea water  
1510 flow taking into account the weight and drag coefficients of all elements of  
1511 the line. The zenith angle  $\Theta$  in one point of the line can be computed from  
1512 the vertical forces  $F_z$  (buoyancy minus weight) and the horizontal drag forces  
1513  $F_{\perp} = \rho C_W A v^2 / 2$ , where  $\rho$  is the water density,  $A$  is the cross-section area  
1514 of the element considered,  $v$  is the sea current velocity, and  $C_W$  is the drag  
1515 coefficient. The drag coefficient was determined by a hydro-dynamical study  
1516 of the storey in the IFREMER pool facility. Since  $\tan(\Theta) = dr/dz$ , the radial  
1517 displacement  $r$  as a function of the vertical coordinate  $z$  can be obtained by  
1518 integration along the line, resulting in the expression:

$$r(z) = av^2z - bv^2 \ln[1 - cz], \quad (4)$$

1519 where  $a$ ,  $b$  and  $c$  are known constants, and the horizontal components of the  
1520 sea current velocity  $v^2 = v_x^2 + v_y^2$  are treated as free fitting parameters. The  
1521 values of sea current velocity inferred from the reconstructed shapes of the  
1522 different lines can be compared among themselves and to the measurements  
1523 provided by the ADCP installed on the instrumentation line in order to have  
1524 a test of the accuracy of the reconstruction procedure.

1525 The measurements with the acoustic positioning system are performed as  
1526 follows. Acoustic sinusoidal wave packets of short duration (typically 2 ms)  
1527 are broadcasted from the emitters at the bottom of each line and detected  
1528 by the hydrophones installed on all lines. Various fixed frequencies between  
1529 40 and 60 kHz are used in turn to differentiate the sound emissions and to  
1530 avoid possible interference due to successive emissions of acoustic waves with  
1531 the same frequency. Detection of the acoustic signal by the hydrophones is  
1532 done by comparison of the amplitude of the numerically filtered signal to a  
1533 preset threshold. The gain of the preamplification as well as the detection

1534 threshold are set for each receiver depending on the emission cycle, the emis-  
1535 sion frequency and the attenuation due to the distances travelled. In this  
1536 way the travel time between the emitter and the receiver can be determined  
1537 independently. Knowing the sound velocity profile, the distance between  
1538 one emitter and one receiver is deduced from the travel time measurement.  
1539 Positions of all hydrophones and transducers are then computed from the  
1540 measured distances using the triangulation principle and a least-mean-square  
1541 minimization procedure.

1542 Prior to positioning measurements, configuration messages are sent from  
1543 the shore station to all acoustic modules. The configuration defines whether  
1544 modules will act as receivers or, in the case of the devices at the bottom of the  
1545 lines, as emitters for a given measurement cycle. In addition the frequency  
1546 and the detection gain are set. The emission of acoustic signals is triggered by  
1547 a synchronization signal sent by the master clock system. The timestamp of  
1548 each detected signal is obtained by starting a counter in the acoustic module  
1549 with the synchronization signal, and by stopping the counter when the signal  
1550 is detected. The accuracy of this counter is 100 ns.

1551 Autonomous transponders installed around the detector are used in the  
1552 measurements in order to enlarge the triangulation basis. These transponders  
1553 are autonomous emitter-receiver beacons fixed on pyramidal structures an-  
1554 chored on the seabed and powered by batteries. Each transponder responds  
1555 at one unique frequency whilst the interrogation occurs at a common commu-  
1556 nication frequency. The transponders can thus be activated and de-activated  
1557 by a transceiver using an acoustic modem dialogue.

1558 The acoustic travel times have to be corrected for the delays of the signal  
1559 due to emission and detection delays including the frequency-matching nu-  
1560 merical filter. Such delays depend on the ratio between the detection thresh-  
1561 old and the measured signal amplitude. The global delay has been measured  
1562 and found to be in the range from 140 to 180  $\mu\text{s}$ . They can be modelled  
1563 according to a third-order polynomial. This polynomial correction is then  
1564 applied to the detection timestamp. The accuracy of the acoustic travel time  
1565 measurement is primarily determined by the jitter of the detected signal.  
1566 This jitter has been measured to be less than 4  $\mu\text{s}$  corresponding to a dis-  
1567 tance of 6 mm for a sound velocity of 1500  $\text{m s}^{-1}$ , even in the presence of a  
1568 30 dB white-noise background.

1569 For the determination of distances from the measurement of the acoustic  
1570 travel time, the knowledge of the sound velocity within the detector is needed.  
1571 The detector is equipped with several Sound Velocimeters (SV) placed at

1572 different locations along the detector lines, in order to determine the sound  
1573 velocity and its variations. In sea water, the sound velocity depends on ther-  
1574 modynamic parameters such as the conductivity, the temperature and the  
1575 pressure, which depend on the depth. Sound velocity can be inferred by  
1576 combined measurements of these quantities performed with a CTD detec-  
1577 tor (conductivity, temperature and depth probes), according to the Chen &  
1578 Millero model [18, 19]. One SV-CTD has been also installed in the apparatus  
1579 in order to have independent sound velocity determination, and also to get  
1580 an estimation of the salinity and temperature gradients within the detector.

1581 The behaviour of the positioning system using the first ANTARES data is  
1582 described in [20, 21]. As an example, Figure 33 shows the x-y displacement in  
1583 the horizontal plane of the five hydrophones at different heights along a line  
1584 as a function of time for a period of 6 months (from July to December 2007).  
1585 A detailed analysis of the system performance indicates that the resolution  
1586 is better than the 20 cm specification at which value it does not degrade the  
angular resolution.

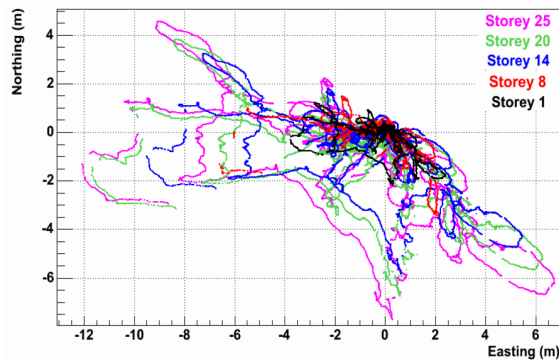


Figure 33: Displacements in the horizontal plane of the five storeys equipped with positioning hydrophones of a line as determined by the positioning system.

1587

#### 1588 6.4.2. Timing calibration

1589 The timing calibration [22] can be divided in two parts. On one hand,  
1590 the master clock which provides a common synchronization signal to the  
1591 whole apparatus can be used to measure the time path from shore to each  
1592 electronics module. This information is useful to check the overall stability  
1593 of the system and to measure the *in situ* time delays after the connection  
1594 of a detector line. Figure 34 shows the round trip time measured for one

1595 electronics module. The stability and accuracy of the measurements are at  
1596 the sub-nanosecond level, as required.

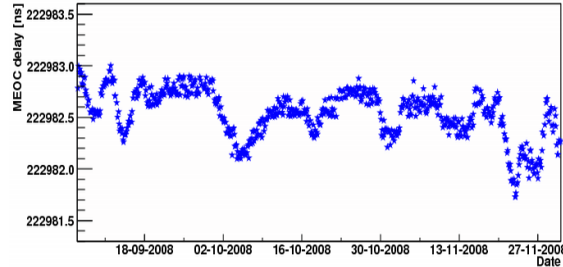


Figure 34: Measurement of the round trip time for clock signals between shore and one of the electronics module of the apparatus.

1597 The time offsets for each specific channel are then calibrated *in situ* by  
1598 means of the optical beacons installed on the lines and the LED pulsers  
1599 mounted inside each Optical Module. The list of optical beacons include LED  
1600 beacons, distributed at different levels along each line, and two laser beacons  
1601 located at the bottom of two central lines. These devices are operated in a  
1602 similar way. While the laser beacons are mainly used for cross-check of the  
1603 timing calibration of the OMs of different lines, the LED beacons remain the  
1604 main tool for *in situ* timing calibration. These beacons are flashed in turn for  
1605 short time periods in order to illuminate the surrounding optical modules.  
1606 From the comparison between the measured and the expected time of the  
1607 hits, taking into account the propagation time of the light, one can infer the  
1608 time offset for each OM.

1609 Figure 35 shows the time residual distribution for one particular OM ob-  
1610 tained from one calibration run. The tail on the right part of the distribution  
1611 can be attributed to light scattering. The position of the leading edge can be  
1612 determined with a Gaussian fit to the left part of the distribution, which is  
1613 less affected by scattering. The distribution of the leading edge as a function  
1614 of the distance (or, equivalently, the storey number) shows a linear trend,  
1615 which is ascribed to the “early-photon effect”. This effect is due to the du-  
1616 ration of the light pulse ( $\text{FWHM} \approx 4 \text{ ns}$ ) and the intensity of the detected  
1617 light. The closer the OM, the more light it receives and therefore the sooner  
1618 the PMT signal passes the preset threshold of the ARS, an effect which is  
1619 further emphasized by time walk. A straight line fit is then applied to the  
1620 data and deviations from this fit are understood as the corrections to be  
1621 made on the time offsets obtained by the calibration onshore. An example

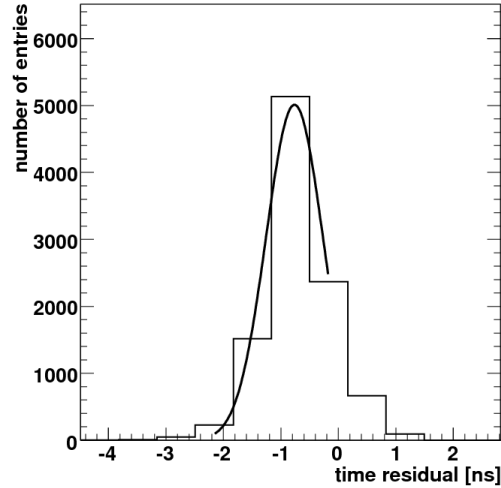


Figure 35: Time residual distribution of the signals in an OM located two storeys above a flashing LED Beacon. The curve is a Gaussian fit with a sigma of 0.5 ns.

is given in Figure 36. In most cases these corrections are small, and only for

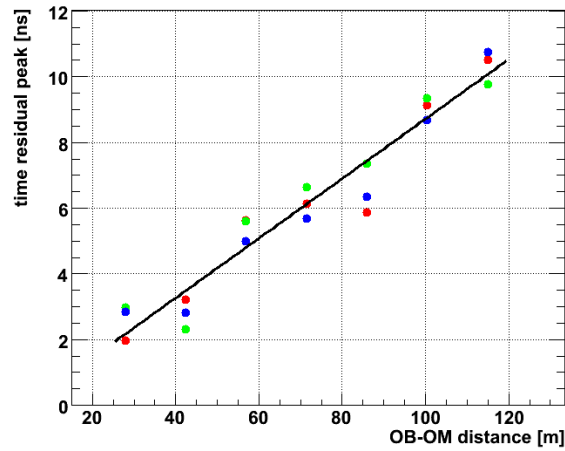


Figure 36: Time residual peak position as a function of the distance between a flashing LED beacon and the OMs along seven storeys above. The three points at each distance correspond to the three OMs in each storey. The additional delay with distance is due to the early photon effect.

1622

1623  $\approx 15\%$  of cases they are larger than 1 ns. This method provides an average

1624 improvement of  $\approx 0.5$  ns over the timing calibration performed onshore.

1625 The time offset variations of each optical module, due to variations in  
1626 the transit time of the photomultiplier for instance, can be monitored by  
1627 operating the LED pulser placed in each optical module. These data show a  
1628 good stability of the time delays when the HV of the PMT and the settings  
1629 of the ARS are not changed.

1630 An additional check of the timing calibration accuracy may come from  
1631 the detection of coincidences of PMT signals induced by Potassium-40 decays  
1632 ( $^{40}\text{K}$ ). This radioactive isotope is naturally present in the sea water. From  
1633 its decay, electrons with a kinetic energy up to 1.3 MeV are produced. This  
1634 energy exceeds the Cherenkov threshold for electrons in water (0.26 MeV),  
1635 and is sufficient to produce up to 150 Cherenkov photons. If the decay occurs  
1636 in the vicinity of a detector storey, a coincident signal may be recorded by a  
1637 pair of PMTs. In Figure 37 the distribution of the measured time difference  
1638 between hits in neighbouring PMTs of one storey is shown. The peak around  
1639 0 ns is mainly due to single  $^{40}\text{K}$  decays producing coincident signals. The  
1640 fit to the data is the sum of a Gaussian distribution and a flat background.  
1641 The full width at half maximum of the Gaussian function is about 9 ns. This  
1642 width is mainly due to the spatial distribution of the  $^{40}\text{K}$  decays around the  
1643 storey. The positions of the peaks of the time distributions for different pairs  
1644 of PMTs in the same storey are used to cross-check the time offsets computed  
1645 with the timing calibration. This is illustrated in Figure 38 which shows a  
1646 comparison of the time offsets calculated from the optical beacon calibration  
1647 and those extracted from the analysis of  $^{40}\text{K}$  coincidences. The rms of the  
1648 distribution is about 0.6 ns.

1649 The coincidences induced by  $^{40}\text{K}$  decays provide also a powerful tool for  
1650 monitoring the relative efficiencies of the individual OM, with an accuracy  
1651 of about 5%.

### 1652 *6.4.3. Amplitude calibration*

1653 Amplitude calibration of each channel is routinely performed. During  
1654 special runs, the output signal of the PMT is digitized at random times.  
1655 This allows for a measurement of the corresponding pedestal value of the  
1656 AVC channel. The single photoelectron peak is studied with minimum bias  
1657 events. The optical activity due the  $^{40}\text{K}$  decays and bioluminescent bacteria  
1658 produces primarily single photons at the photocathode level. The knowledge  
1659 of the position of the single photoelectron peak and of the pedestal is used to  
1660 determine the charge conversion over the full dynamical range of the ADC.



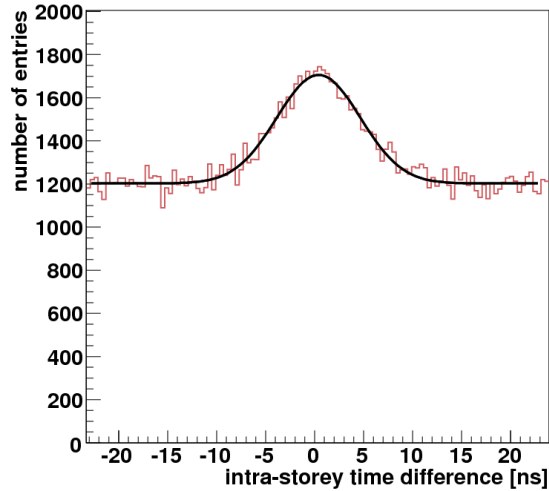


Figure 37: Time difference between signals measured by a pair of PMTs in storey 1 of line 1. The peak is due to single  $^{40}\text{K}$  decays, whereas the flat background is due to accidental coincidences of  $^{40}\text{K}$  decays and bioluminescence. The solid line is a fit of the sum of a Gaussian distribution and a flat background to the data.

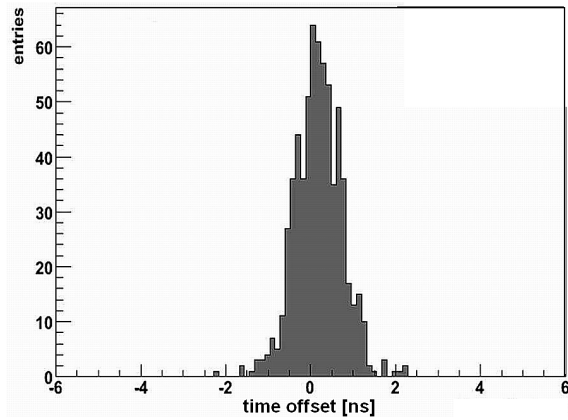


Figure 38: Differences between the time offsets inferred from the calibrations with the LED beacons and independently determined by the  $^{40}\text{K}$  coincidence method for all photomultiplier tubes.

1661 The charge measurements, performed inside the ARS, appear to be influenced  
 1662 by the time measurements in the TVC channel (the inverse effect does not  
 1663 apply). This cross-talk effect is corrected on an event-by-event basis. The  
 1664 maximal size of this correction amounts to 0.2 photoelectrons. The effect is

1665 thought to be due to a coupling between the capacitors inside the pipeline in  
1666 the chips. This correction is inferred with *in situ* measurements of the AVC  
1667 value versus the TVC value.

1668 Once the cross-talk correction is made, the charge calibration is applied  
1669 to reconstruct the amplitude of the individual signals detected from the op-  
1670 tical modules. As shown in Figure 39, this distribution is peaked at one  
1671 photoelectron as expected from  $^{40}\text{K}$  decay and bioluminescence.

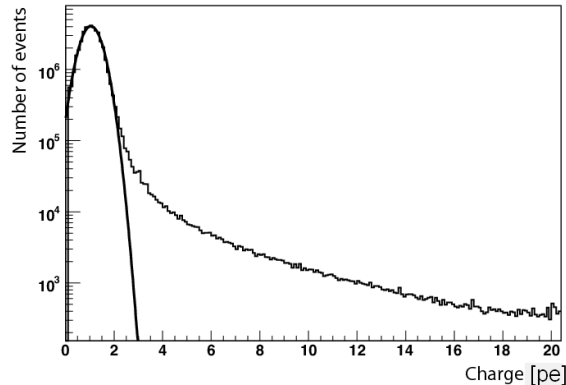


Figure 39: Calibrated charge distribution combining all PMTs in the detector.

1672 The front-end chip has also the capability to perform full waveform sam-  
1673 pling (WF) of the PMT signal in addition to the charge measurement of  
1674 the PMT pulse and its arrival time. This functionality is primarily meant  
1675 for recording double pulses or large amplitude signals. However, it is also  
1676 exploited during the calibration in order to cross-check the computation of  
1677 the charge by the integrator circuit of the front-end chip and for determining  
1678 the shape of the SPE signals in order to correct for the so-called walk effect  
1679 (i.e., the dependence of the threshold crossing time on the signal amplitude).

### 1680 6.5. Performance of the apparatus

1681 There are a number of criteria which can be considered for assessing the  
1682 performance of a complex apparatus like ANTARES. The first criterion con-  
1683 cerns stability of the operating conditions. The junction box has the longest  
1684 operation history since it was installed in December 2002. Temperature and  
1685 relative humidity inside the junction box have been continuously logged dur-  
1686 ing this period by a battery-powered monitor system. A sample of such  
1687 measurements, taken during the first years of operation, is shown in Fig-  
1688 ure 40. The relative humidity is seen to plateau at 50% when the detector

1689 is not powered and to drop during periods when the junction box is warm  
 1690 with the transformer powered for the operation of prototype detection lines.

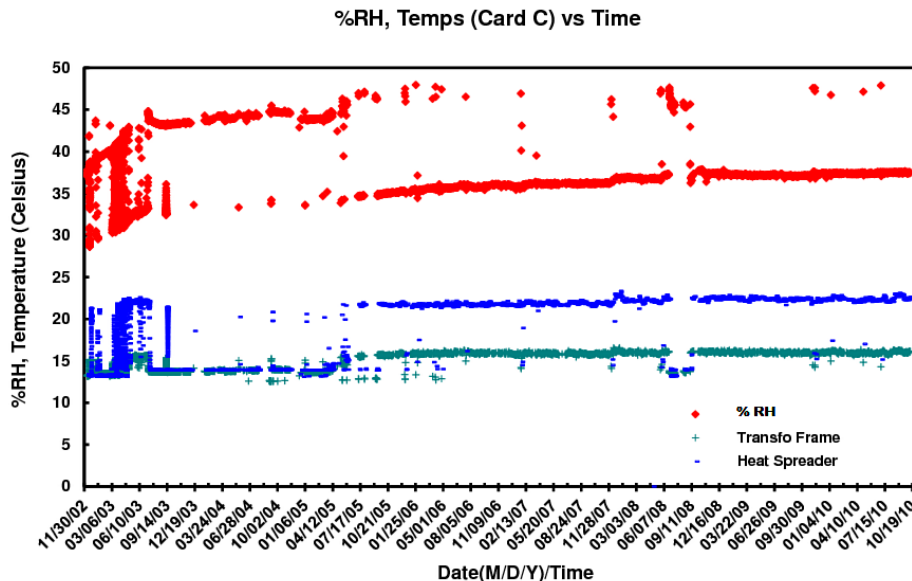


Figure 40: Long-term monitor of relative humidity (RH) (top curve) and temperature (bottom curves) in the underwater junction box over a period of eight years. From 2002 to 2005, during the prototyping phase, the detector was powered off a large part of the time while from 2006, with operational detector lines, the power was mostly on. The two temperature curves come from probes located at different positions in the junction box.

1691 Another important parameter for assessing the apparatus performance  
 1692 is the fraction of time dedicated to data taking. This should be as high as  
 1693 possible in order to maximize the statistics of events collected and to allow for  
 1694 a maximum probability of detecting transient phenomena. Since the start  
 1695 of the operation of the detector in March 2006, the data taking live time  
 1696 has been better than 90 %, the larger fractions of dead time being due to  
 1697 construction/maintenance activities ( $\approx 4\%$ ) and calibrations ( $\approx 3\%$ ). The  
 1698 trigger rate, which is dominated by cosmic ray muons, is at the level of a few  
 1699 tens of Hz. Neutrino events are recorded at a rate of about four per day.

1700 Detection efficiency and angular resolution are the parameters which  
 1701 mainly determine the apparatus sensitivity to neutrino sources; neutrino en-  
 1702 ergy resolution is also significant, as it helps to discriminate between neu-  
 1703 trinos of astrophysical origin and those created in cosmic ray showers in  
 1704 the atmosphere. These three parameters have been studied using a detailed

1705 Monte Carlo simulation of the detector response to muons and neutrinos. The  
1706 performance of the apparatus has been reported in references [23, 24, 25].

1707 Angular resolution, which is a key element for separating a point source  
1708 neutrino signal from the atmospheric neutrino background, depends on the  
1709 timing resolution, the accuracy of the OM positioning system and the water  
1710 scattering properties. Detection efficiency is affected by different factors,  
1711 the most significant being the light transmission parameters in water and  
1712 the OM detection efficiency; the latter in turn depends on several factors  
1713 such as light transmission losses, photocathode quantum efficiency, electron  
1714 collection efficiency and the threshold setting.

1715 An example of an energetic upgoing neutrino candidate event, observed  
1716 on eight ANTARES detector lines is shown in Figure 41. For each detector  
1717 line, a panel shows the vertical position (y-axis) and the arrival time of the  
1718 hits (x-axis). In this coordinates system, the hits must lie on a hyperbola.  
1719 A reconstruction algorithm [27] is applied and the curves show the results of  
1720 the best fit. The “aperture” of the asymptotes is related to the angle of the  
1721 muon with respect to the detector line and the “summit” gives the altitude  
1722 of the closest approach of the muon to the line.

1723 In Figure 42 the time residuals of the track fits for data and Monte Carlo  
1724 simulation are shown. A minimum number of 15 hits used in the fit is  
1725 required. Good agreement can be seen between the data and the simulation  
1726 with a core timing resolution of 2 ns, obtained by fitting a Gaussian to the  
1727 data in a range of values between residuals from -4 ns to 4 ns. The tail of  
1728 late hits is attributed to light scattering and to the presence of showers in  
1729 the track sample.

1730 In the absence of a point-like source, demonstration of the experimental  
1731 angular resolution and absolute pointing of the detector can be provided by  
1732 observation of the moon shadow with cosmic rays. However several years of  
1733 data taking will be needed. A program is also planned to look for events  
1734 detected in coincidence by the apparatus and by an array of scintillators  
1735 floating on the sea surface above [28].

1736 In Figure 43 is shown the measured elevation distribution of selected  
1737 events. Also shown is the corresponding expectation from the Monte Carlo  
1738 simulation, which takes into account the best measurements and estimates of  
1739 the contributions to detector efficiency mentioned above. The overall agree-  
1740 ment between data and Monte Carlo is well within the estimated systematic  
1741 uncertainties of about 20 % for the detector effects and an additional 30 %  
1742 of uncertainty on the absolute flux of atmospheric particles.

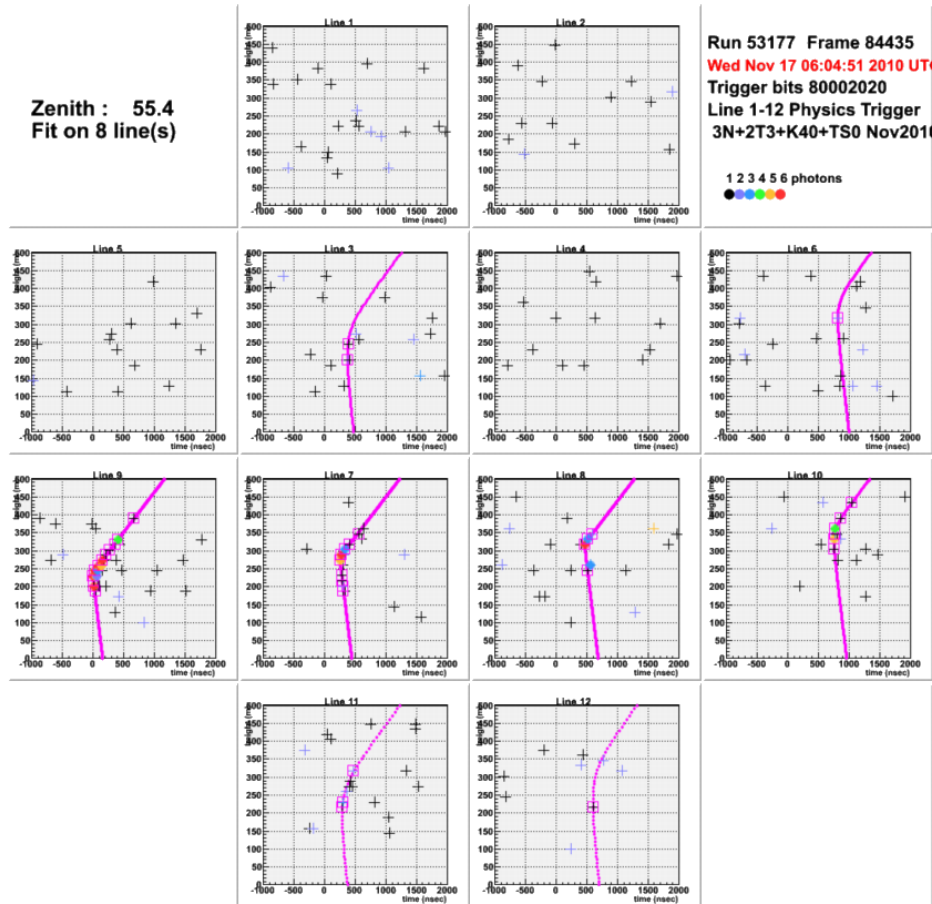


Figure 41: A graphical representation of a neutrino-induced event. For each detector line, a panel shows the vertical position (y-axis) and the arrival time of the hits (x-axis). The panels are arranged so as to reproduce the relative positions of the lines in the apparatus. Crosses are hits in a time window of 3 microseconds around the trigger; full circles are hits passing the trigger condition; open boxes are hits used in the final fit. The symbols are coloured, according to the illustrated code, based on the hit amplitude. The final fit is used to draw the pink lines.

1743 A further check of the efficiency assumptions in the Monte Carlo, inde-  
 1744 pendently of the absolute flux of particles, is shown in Figure 44. Here the  
 1745 number of hits associated to the fitted tracks is compared to the Monte Carlo  
 1746 expectation for the upward going events of Figure 43. A good agreement be-  
 1747 tween data and Monte Carlo is observed.

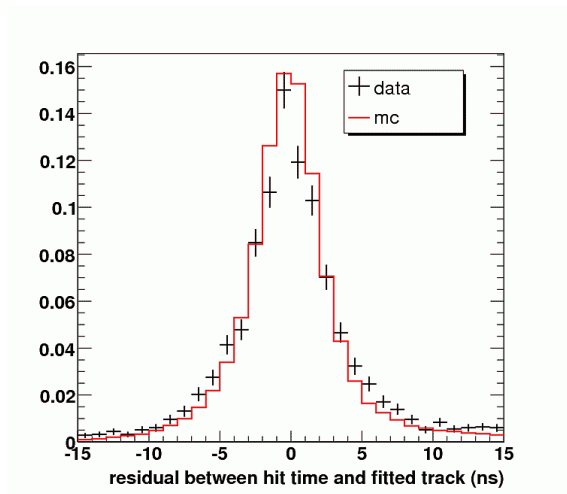


Figure 42: Time residuals for tracks of neutrino candidate events as measured from the data (black crosses) and as expected from the simulation (red histogram).

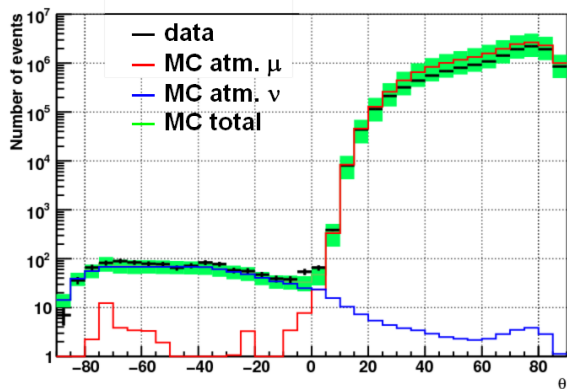


Figure 43: Elevation distribution of events.

## 1748 7. Conclusions

1749 After an extensive period of R&D and prototyping, the construction of  
 1750 ANTARES has been successfully completed. The high energy neutrino tele-  
 1751 scope consisting of 12 lines holding optical modules is deployed on the seabed  
 1752 off the Toulon coast at 2475 m depth. Since the deployment of the first line  
 1753 in 2006, data taking has proceeded essentially continuously.

1754 The methods and the procedures to control such a novel detector have  
 1755 been developed including *in situ* timing calibration, acoustic positioning of

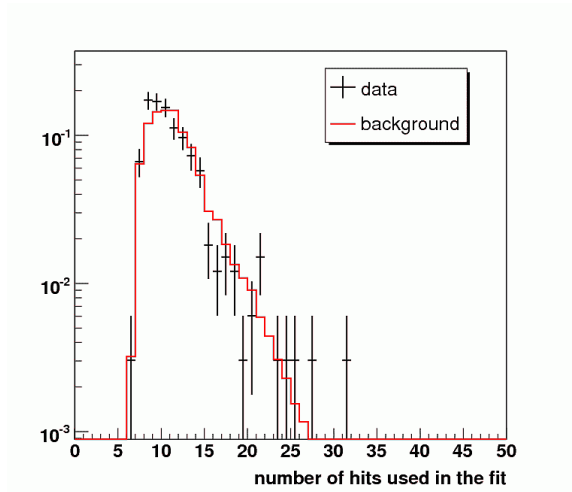


Figure 44: Number of hits in neutrino candidate events as measured from the data (black crosses) and as expected from the simulation (red histogram). The two distributions have been normalized to the same event count.

1756 the detector elements and charge calibration.

1757 All the design goals of the detector have been attained. The measure-  
 1758 ments of the position of the optical modules is achieved to accuracy better  
 1759 than 20 cm and the expected time resolution of 1 ns is reached. This allows  
 1760 the reconstruction of the events with the desired angular resolution.

1761 ANTARES has demonstrated that undersea neutrino telescopes are fea-  
 1762 sible and manageable from the onshore infrastructure. The successful oper-  
 1763 ation of ANTARES represents an important step towards a future km<sup>3</sup>-scale  
 1764 high-energy neutrino observatory and marine sciences infrastructure.

1765

1766 We dedicate this paper to the memory of our colleague and friend Patrice  
 1767 Payre, who passed away during the preparation of this paper.

## 1768 Acknowledgements

1769 The authors acknowledge the financial support of the funding agencies:  
 1770 Centre National de la Recherche Scientifique (CNRS), Commissariat à l'énergie  
 1771 atomique et aux énergies alternatives (CEA), Agence Nationale de la Recherche  
 1772 (ANR), Commission Européenne (FEDER fund and Marie Curie Program),  
 1773 Région Alsace (contrat CPER), Région Provence-Alpes-Côte d'Azur, Dépar-  
 1774 tement du Var and Ville de La Seyne-sur-Mer, France; Bundesministerium

1775 für Bildung und Forschung (BMBF), Germany; Istituto Nazionale di Fisica  
1776 Nucleare (INFN), Italy; Stichting voor Fundamenteel Onderzoek der Materie  
1777 (FOM), Nederlandse organisatie voor Wetenschappelijk Onderzoek (NWO),  
1778 the Netherlands; Council of the President of the Russian Federation for young  
1779 scientists and leading scientific schools supporting grants, Russia; National  
1780 Authority for Scientific Research (ANCS), Romania; Ministerio de Ciencia e  
1781 Innovación (MICINN), Prometeo of Generalitat Valenciana and MultiDark,  
1782 Spain. We also acknowledge the technical support of Ifremer, AIM and Fos-  
1783 elev Marine for the sea operation and the CC-IN2P3 for the computing fa-  
1784 cilities.



1785 **List of Figures**

1786	1	Principle of detection of high energy muon neutrinos in an underwater neutrino telescope. The incoming neutrino interacts with the material around the detector to create a muon. The muon gives Cherenkov light in the sea water which is then detected by a matrix of light sensors. The original spectrum of light emitted from the muon is attenuated in the water such that the dominant wavelength range detected is between 350 and 500 nm. . . . .	12
1787			
1788			
1789			
1790			
1791			
1792			
1793			
1794	2	Schematic view of the ANTARES detector. . . . .	13
1795	3	Schematic view of the data acquisition system. The dashed line boxes refer to hardware devices, the ellipses correspond to processes running on those devices. The lines between processes indicate the exchange of information (commands, data, messages, etc.). . . . .	15
1796			
1797			
1798			
1799			
1800	4	Schematic view of an optical module . . . . .	20
1801	5	Results of dark count rate (top) and peak/valley ratio (bottom) for the full set of tested PMTs. . . . .	20
1802			
1803	6	Measured mean pulse height of single photoelectrons for each PMT at nominal gain. . . . .	21
1804			
1805	7	Photograph of an optical module. It is positioned on a mirror to better show the full assembly. . . . .	25
1806			
1807	8	OM support mechanics. . . . .	26
1808	9	OMF equipped with the 3 OMs, the LCM and an LED beacon. The mechanical parts used for fixing cables toward the upper and the lower storeys are omitted. . . . .	27
1809			
1810			
1811	10	The ARS_MB board with the 2 ARSs (labelled 16 and 15). The 3 <sup>rd</sup> one (top right, labelled 12) is foreseen for trigger purposes. . . . .	29
1812			
1813			
1814	11	The DAQ/SC board holding the processor (centre), the FPGA (left) and the optical link to the MLCM (right). . . . .	30
1815			
1816	12	The COMPASS_MB equipped with a TCM2 sensor on a raised daughter card. . . . .	31
1817			
1818	13	The DWDM board. . . . .	32
1819	14	The crate of an MLCM equipped with the electronics boards. . . . .	33

1820	15	Cross section of the EMC. From centre to outside one can	
1821		distinguish the layer with 3 tubes, each housing 7 optical fi-	
1822		bres, the layer with 9 copper conductors, the LDPE jacket,	
1823		the aramid braid and the polyurethane sheath. The external	
1824		diameter is 30 mm. . . . .	33
1825	16	Mechanical termination of an EMC. . . . .	34
1826	17	EMC penetrators of the LCM container. Left: non water	
1827		blocking. Right: water blocking. For clarity, the 3rd fibre	
1828		tube and the 9 conductors are not shown. . . . .	35
1829	18	The ANTARES Bottom String Structure. . . . .	36
1830	19	The SCM_WDM board. . . . .	39
1831	20	Line shape for a sea current velocity of 25 cm s <sup>-1</sup> velocity.	
1832		The horizontal scale is enhanced to better illustrate the line	
1833		shape. . . . .	42
1834	21	The electronic boards and light sources of an LED beacon. . .	43
1835	22	Components of the laser beacon. . . . .	44
1836	23	The instrumentation line IL07. Elements are indicated schemat-	
1837		ically; not drawn to scale. . . . .	46
1838	24	A schematic view of the complete link between the SPM/SCM	
1839		container of a line and the JB container. . . . .	48
1840	25	The junction box container and its support frame. . . . .	49
1841	26	Junction box on the deck of the deployment ship. . . . .	50
1842	27	Junction box output breaker management. . . . .	51
1843	28	View inside the open JB: heat-spreader disk, transformer con-	
1844		nections and primary circuit current sensor, passive fibre optic	
1845		splitters and cassettes protecting fibre fusion splices. . . . .	52
1846	29	Sections of the undersea cable. . . . .	54
1847	30	Electro-optical plug and receptacle for connection of the un-	
1848		dersea cable to the junction box. . . . .	55
1849	31	Power distribution system from the shore to the underwater	
1850		junction box. . . . .	56
1851	32	Definitions of the symbols used in equation 2 (left) and in	
1852		equation 3 (right). . . . .	65
1853	33	Displacements in the horizontal plane of the five storeys equipped	
1854		with positioning hydrophones of a line as determined by the	
1855		positioning system. . . . .	69
1856	34	Measurement of the round trip time for clock signals between	
1857		shore and one of the electronics module of the apparatus. . . .	70

1858	35	Time residual distribution of the signals in an OM located two storeys above a flashing LED Beacon. The curve is a Gaussian fit with a sigma of 0.5 ns. . . . .	71
1859			
1860			
1861	36	Time residual peak position as a function of the distance between a flashing LED beacon and the OMs along seven storeys above. The three points at each distance correspond to the three OMs in each storey. The additional delay with distance is due to the early photon effect. . . . .	71
1862			
1863			
1864			
1865			
1866	37	Time difference between signals measured by a pair of PMTs in storey 1 of line 1. The peak is due to single $^{40}\text{K}$ decays, whereas the flat background is due to accidental coincidences of $^{40}\text{K}$ decays and bioluminescence. The solid line is a fit of the sum of a Gaussian distribution and a flat background to the data. . . . .	73
1867			
1868			
1869			
1870			
1871			
1872	38	Differences between the time offsets inferred from the calibrations with the LED beacons and independently determined by the $^{40}\text{K}$ coincidence method for all photomultiplier tubes. . . .	73
1873			
1874			
1875	39	Calibrated charge distribution combining all PMTs in the detector. . . . .	74
1876			
1877	40	Long-term monitor of relative humidity (RH) (top curve) and temperature (bottom curves) in the underwater junction box over a period of eight years. From 2002 to 2005, during the prototyping phase, the detector was powered off a large part of the time while from 2006, with operational detector lines, the power was mostly on. The two temperature curves come from probes located at different positions in the junction box. . . . .	75
1878			
1879			
1880			
1881			
1882			
1883			
1884	41	A graphical representation of a neutrino-induced event. For each detector line, a panel shows the vertical position (y-axis) and the arrival time of the hits (x-axis). The panels are arranged so as to reproduce the relative positions of the lines in the apparatus. Crosses are hits in a time window of 3 microseconds around the trigger; full circles are hits passing the trigger condition; open boxes are hits used in the final fit. The symbols are coloured, according to the illustrated code, based on the hit amplitude. The final fit is used to draw the pink lines. . . . .	77
1885			
1886			
1887			
1888			
1889			
1890			
1891			
1892			
1893			

1894	42	Time residuals for tracks of neutrino candidate events as measured from the data (black crosses) and as expected from the simulation (red histogram). . . . .	78
1895			
1896			
1897	43	Elevation distribution of events. . . . .	78
1898	44	Number of hits in neutrino candidate events as measured from the data (black crosses) and as expected from the simulation (red histogram). The two distributions have been normalized to the same event count. . . . .	79
1899			
1900			
1901			

1902 **List of Tables**

1903	1	Data on the OM glass sphere. . . . .	21
1904	2	Tension (kN) at the bottom of the specified cable or chain, for 3 periods in the life of the line and at 8 positions along the line.	41
1905			
1906	3	List of the instruments on the line IL07. . . . .	45
1907	4	Characteristics of the undersea cable. . . . .	54
1908	5	Layout of the undersea cable. . . . .	55

1909 **References**

1910 [1] H. Hanada et al., *A Highly Sensitive Optical Detector for a Use in Deep*  
1911 *Underwater*, Nucl. Instr. and Meth. A408 (1998) 425-437.

1912 [2] G. V. Domogatsky et al., [Baikal Collaboration], *The Lake Baikal Deep*  
1913 *Underwater Detector*, Nucl. Phys. Proc. Suppl. **19** (1991) 388-395.

1914 [3] E. Andrés et al., *The AMANDA neutrino telescope: principle of operation*  
1915 *and first results*, Astrop. Phys. 13 (2000) 1-20.

1916 [4] J.A. Aguilar et al., *Background light in potential sites for the ANTARES*  
1917 *undersea neutrino telescope*, Astrop. Phys. 13 (2000) 127-136, astro-  
1918 ph/9910170.

1919 [5] J.A. Aguilar et al., *Sedimentation and Fouling of Optical Surfaces at the*  
1920 *ANTARES Site*, Astrop. Phys. 17 (2003) 253-267, astro-ph/0206454.

1921 [6] J.A. Aguilar et al., *Transmission of light in deep sea water at the site of*  
1922 *the Antares neutrino telescope*, Astrop. Phys. 23 (2005) 131-155, astro-  
1923 ph/0412126.

- 1924 [7] J.A. Aguilar et al., *AMADEUS The Acoustic Neutrino Detection Test*  
1925 *System of the ANTARES DeepSea Neutrino Telescope*, accepted for  
1926 publication in Nucl. Instr. and Meth., doi:10.1016/j.nima.2010.09.053,  
1927 arXiv:1009.4179.
- 1928 [8] J.A. Aguilar et al., *The data acquisition system for the ANTARES neu-*  
1929 *trino telescope*, Nucl. Instr. and Meth. A570 (2007) 107-116.
- 1930 [9] J.A. Aguilar et al., *Performance of the front-end electronics of the AN-*  
1931 *TARES neutrino telescope*, Nucl. Instr. and Meth. A622 (2010) 59-73,  
1932 arXiv:1007.2549.
- 1933 [10] M. Amram et al., *The ANTARES optical module*, Nucl. Instr. and Meth.  
1934 A484 (2002) 369-383.
- 1935 [11] J.A. Aguilar et al., *Study of large hemispherical photomultiplier tubes for*  
1936 *the ANTARES neutrino telescope*, Nucl. Instr. and Meth. A555 (2005)  
1937 132-141.
- 1938 [12] P.W. Gorham et al., *Mechanical and Acoustic*  
1939 *Studies of Deep Ocean Glass Sphere Implosions*,  
1940 <http://www.phys.hawaii.edu/~dumand/implopp.ps>.
- 1941 [13] Cockcroft J.D. and Walton E.T.S. (1932). Proc. R. Soc. London  
1942 A137:229.
- 1943 [14] M. Ageron et al., *The Antares optical beacon system*, Nucl. Instr. and  
1944 Meth. A578 (2007) 498-509, astro-ph/0703335.
- 1945 [15] J.A. Aguilar et al., *First results of the Instrumentation Line for the*  
1946 *deep-sea ANTARES neutrino telescope*, Astroparticle Physics 26 (2006)  
1947 314-324, astro-ph/0606229.
- 1948 [16] R. Gurin and A. Maslennikov, *Controlhost: Distributed data handling*  
1949 *package*. Technical report, CASPUR Inter-University Computing Con-  
1950 sortium Rome, 1995.
- 1951 [17] M. Bringer et al., *The TAROT observatory data management*, Astron.  
1952 Astrophys. Suppl. Ser. 138 (1999) 581-582.
- 1953 [18] C-T. Chen and F.J. Millero, *Speed of sound in seawater at high pressures*,  
1954 (1977) J. Acoust. Soc. Am. 62(5) 1129-1135.

- 1955 [19] *The Practical Salinity Scale 1978 and the International Equation of State*  
1956 *of Seawater 1980*, UNESCO technical papers in marine science 36.
- 1957 [20] P. Keller (for the ANTARES Collaboration), *Acoustic Positioning Sys-*  
1958 *tem for the Deep-sea ANTARES Neutrino Telescope*, in Proc. UNWAT  
1959 - SENSORCOMM Conf., Valencia, 2007, 243-247.
- 1960 [21] M. Ardid (for the ANTARES Collaboration), *Positioning system of the*  
1961 *ANTARES neutrino telescope*, Nucl. Instr. and Meth. A602 (2009) 174-  
1962 176.
- 1963 [22] J.A. Aguilar et al., *Time Calibration of the ANTARES Neutrino Tele-*  
1964 *scope*, Astrop. Phys. 34 (2011) 539-549, [arXiv:1012.2204]
- 1965 [23] M. Ageron et al., *Performance of the First ANTARES Detector Line*,  
1966 Astrop. Phys. 31, 4 (2009) 277-283.
- 1967 [24] J.A. Aguilar et al., *Measurement of the atmospheric muon flux with a*  
1968 *4 GeV threshold in the ANTARES neutrino telescope*, Astrop. Phys. 33  
1969 (2010) 86-90, astro-ph/0910.4843.
- 1970 [25] J.A. Aguilar et al., *Zenith distribution and flux of atmospheric muons*  
1971 *measured with the 5-line ANTARES detector*, Astrop. Phys. 34 (2010)  
1972 179-184, arXiv:0910.4843.
- 1973 [26] M. Ageron et al., *Studies of a full scale mechanical prototype line for*  
1974 *the ANTARES neutrino telescope and tests of a prototype instrument*  
1975 *for deep-sea acoustic measurements*, Nucl. Instr. and Meth. A581(2007)  
1976 695-708.
- 1977 [27] J.A. Aguilar et al., *A Fast Algorithm for Muon Track Reconstruction and*  
1978 *its Application to the ANTARES Neutrino Telescope*, to be published in  
1979 Astrop. Phys.
- 1980 [28] J.-P. Ernenwein, A. Tsirigotis and S. Tzamarias, *Study of the calibra-*  
1981 *tion potential of HELYCON detectors with ANTARES*, Nucl. Instr. and  
1982 Meth. A602 (2009), 88-90.